HHS Public Access

Author manuscript

Cell Rep. Author manuscript; available in PMC 2023 September 12.

Published in final edited form as:

Cell Rep. 2022 January 18; 38(3): 110264. doi:10.1016/j.celrep.2021.110264.

R-type voltage-gated Ca^{2+} channels mediate A-type K^+ current regulation of synaptic input in hippocampal dendrites

Jonathan G. Murphy[1,3,*], **Jakob J. Gutzmann**[1], **Lin Lin**[1], **Jiahua Hu**[1], **Ronald S. Petralia**[2], **Ya-Xian Wang**[2], **Dax A. Hoffman**[1,*]

[1]Molecular Neurophysiology and Biophysics Section, *Eunice Kennedy Shriver* National Institute of Child Health and Human Development, National Institutes of Health, Bethesda, MD 20892, USA

[2]Advanced Imaging Core, National Institute on Deafness and Other Communication Disorders, National Institutes of Health, Bethesda, MD 20892, USA

[3]Lead contact

SUMMARY

The subthreshold voltage-gated transient K^+ current (I_A) carried by pore-forming Kv4.2 subunits regulates the propagation of synaptic input, dendritic excitability, and synaptic plasticity in CA1 pyramidal neuron dendrites of the hippocampus. We report that the Ca^{2+} channel subunit Cav2.3 regulates I_A in this cell type. We initially identified Cav2.3 as a Kv4.2-interacting protein in a proteomic screen and we confirmed Cav2.3-Kv4.2 complex association using multiple techniques. Functionally, Cav2.3 Ca^{2+}-entry increases Kv4.2-mediated whole-cell current due to an increase in Kv4.2 surface expression. Using pharmacology and Cav2.3 knockout mice, we show that Cav2.3 regulates the dendritic gradient of I_A. Furthermore, the loss of Cav2.3 function leads to the enhancement of AMPA receptor-mediated synaptic currents and NMDA receptor-mediated spine Ca^{2+} influx. These results propose that Cav2.3 and Kv4.2 are integral constituents of an ion channel complex that affects synaptic function in the hippocampus.

In brief

Murphy et al. show that feedback regulation of synaptic input by local Ca^{2+} influx is mediated by a physical and functional coupling between Cav2.3 and Kv4.2 voltage-gated ion channels. Cav2.3 promotes somatodendritic surface expression of Kv4.2 in CA1 pyramidal neurons to limit the magnitude of postsynaptic responses

Graphical abstract

*Correspondence: jonathan.murphy@nih.gov (J.G.M.), hoffmand@mail.nih.gov (D.A.H.) .

AUTHOR CONTRIBUTIONS

Conceptualization, J.G.M., J.J.G., J.H., and D.A.H.; methodology, J.G.M., J.J.G., J.H., and R.S.P.; investigation, J.G.M., J.J.G., L.L., J.H., R.S.P., and Y.-X.W.; writing – original draft, J.G.M.; writing – review & editing, J.G.M., J.J.G., L.L., R.S.P., J.H., and D.A.H.; funding acquisition, J.G.M. and D.A.H.; supervision, D.A.H.

DECLARATION OF INTERESTS

The authors declare no competing interests.

SUPPLEMENTAL INFORMATION

Supplemental information can be found online at https://doi.org/10.1016/j.celrep.2021.110264.

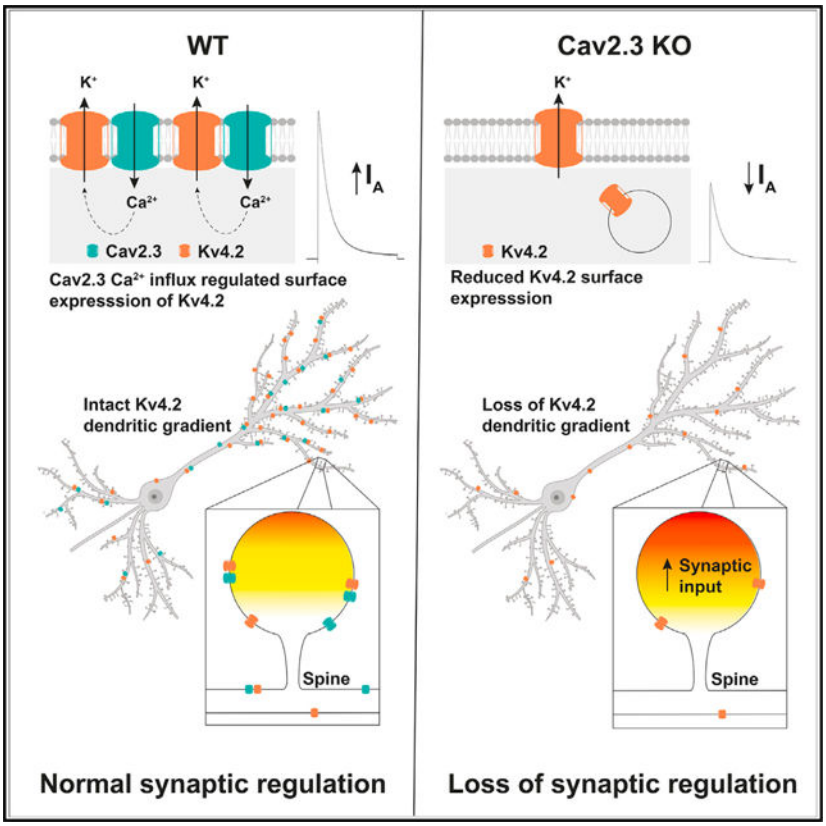

INTRODUCTION

In neuronal dendrites, voltage-gated ion channels modulate the amplitude, propagation, and integration of synaptic input. The voltage-gated K^+ channel subunit Kv4.2 is highly expressed in the dendrites of hippocampal CA1 pyramidal neurons and conducts a low threshold-activated transient outward K^+ current known as A-type current (I_A) (Maletic-Savatic et al., 1995; Sheng et al., 1992). Dendritic I_A regulates synaptic integration, the magnitude of backpropagating action potentials (bAPs), action potential repolarization, and dendritic plateau potentials (Cai et al., 2004; Cash and Yuste, 1998, 1999; Hoffman et al., 1997; Kim et al., 2005; Seong et al., 2014). Kv4.2 regulation of dendritic excitability plays an active role in hippocampal synaptic plasticity and learning (Andrasfalvy et al., 2008; Chen et al., 2006b; Lockridge and Yuan, 2011; Sun et al., 2011; Wang et al., 2013; Watanabe et al., 2002). The dysregulation of I_A has been reported in both animal models and human cases of Alzheimer's disease, epilepsy, autism, and fragile X syndrome (Barnwell et al., 2009; Bernard et al., 2004; Hall et al., 2015; Gross et al., 2011; Guglielmi et al., 2015; Monaghan et al., 2008; Singh et al., 2006). A thorough understanding of the mechanisms underlying neuronal I_A would facilitate the identification of therapeutic targets for neurological disorders.

The typical expression and biophysical properties of Kv4.2-mediated I_A requires binding with auxiliary subunits known as K^+ channel interacting proteins (KChIPs) and dipeptidyl aminopeptidase-like proteins (DPPs), which have profound effects on Kv4.x subunit

expression, stability, and biophysical properties (An et al., 2000; Jerng and Pfaffinger, 2014; Nadal et al., 2003). KChIPs are Ca^{2+}-binding proteins of the neuronal Ca^{2+} sensor (NCS) gene family expressed from four genes (*KCNIP1–4*). KChIPs are highly conserved in their globular core domain (~70%) that contains N and C lobules, each with two EF-hands (EF). KChIPs bind the intracellular N and C terminus of the Kv4.x subunit to stabilize the channel complex and regulate Kv4.x closed state inactivation and recovery from inactivation (Callsen et al., 2005; Kise et al., 2021; Pioletti et al., 2006; Wang et al., 2007). Like the other NCS proteins, divalent metal ion binding is restricted to KChIP EFs 2, 3, and 4. At physiological free Ca^{2+} concentrations in neurons, the Ca^{2+} occupancy at the three Ca^{2+}-binding EF-hands is unknown. However, dynamic Ca^{2+} binding in response to transient Ca^{2+} elevations during neuronal activity is a compelling and largely untested potential Kv4.x feedback mechanism. Ca^{2+} binding to purified KChIP induces global structural changes throughout the protein that may regulate oligomerization and Kv4.x interactions (Craig et al., 2002; Osawa et al., 2001). The effects of Ca^{2+} on the Kv4.x-KChIP complex has been studied using EF-hand mutations or by altering intracellular free Ca^{2+} concentrations (An et al., 2000; Groen and Bahring, 2017; Morohashi et al., 2002; Murphy and Hoffman, 2019; Pioletti et al., 2006). EF-hand mutations potently reduce KChIP regulation of Kv4.x channel trafficking and function, likely disrupting the tertiary structure and Ca^{2+} binding of KChIP. Furthermore, patch-clamp studies of Kv4.x channel function in various neuronal and non-neuronal cell types by the addition of intracellular free Ca^{2+} or Ca^{2+} chelators in the patch pipette have produced variable results that are difficult to interpret (Groen and Bahring, 2017; Chen and Wong, 1991; Murphy and Hoffman, 2019; Patel et al., 2002; Wang et al., 2005). In a similar effort to test the role of elevated intracellular Ca^{2+} on Kv4.x-KChIP function, we recently reported an increase in Kv4.2 current density using a low affinity Ca^{2+} chelator (hydroxyethylethylenediaminetriacetic acid [HEDTA]) in the patch pipette to clamp intracellular free Ca^{2+} at ~10 μM in HEK293-T cells (Murphy and Hoffman, 2019). This effectwas identified in a subset of KChIP isoforms, suggesting that cell-type-specific KChIP expression may be an underappreciated aspect of Ca^{2+} regulation of Kv4.x-KChIP complexes.

Over the last decade, canonically voltage-gated Kv4.x channels have become appreciated as targets of intracellular Ca^{2+} via Ca^{2+} binding KChIP subunits. In the cerebellum, I_A was reportedly regulated by Ca^{2+} entry through T-type voltage-gated Ca^{2+} channels (Cav3.x) in a KChIP-dependent manner that shifted the availability of I_A to more negative membrane potentials and resulted in activity-dependent modulation of cell excitability (Anderson et al., 2010). In hippocampal CA1 pyramidal neurons, Wang and colleagues reported that Cav2.3 (R-type) voltage-gated Ca^{2+} channels function to attenuate the size of evoked excitatory postsynaptic potentials (EPSPs) by promoting Kv4.2 function (Wang et al., 2014). Cav2.3 channels are expressed in the dendrites and spines of CA1 hippocampal pyramidal neurons and regulate action potential afterhyperpolarization and afterdepolarization, the magnitude of bAP-evoked Ca^{2+} transients, and Ca^{2+} influx in spines and dendrites (Bloodgood and Sabatini, 2007; Gutzmann et al., 2019; Magee and Johnston, 1995; Metz et al., 2005; Parajuli et al., 2012; Takahashi and Magee, 2009). Wang et al. disrupted Cav2.3-mediated EPSP boosting using 1,2-bis(*o*-aminophenoxy)ethane-*N*′*N*′*N*′-tetraacetic acid (BAPTA) or a pan-KChIP antibody in the patch pipette suggesting that Cav2.3 and KChIP are in

close proximity (<50 nm). However, the molecular nature of the interaction, whether Kv4.2-KChIP Ca^{2+} regulation in hippocampus is specific to Cav2.3 channels, and a mechanistic explanation for Cav2.3 regulation of I_A remained unknown. Here, we identified a nano-scale interaction between Cav2.3 and Kv4.2 that regulates the amplitude of neuronal I_A to attenuate spontaneous synaptic input through a Kv4.2 surface localization mechanism.

RESULTS

Cav2.3 and Kv4.2 voltage-gated ion channel subunits form a protein complex in the rodent hippocampus

I_A in CA1 pyramidal neurons is conducted by pore-forming Kv4.2 subunits in association with KChIP and DPP accessory subunits, which were identified nearly two decades ago (An et al., 2000; Nadal et al., 2003). We used tandem affinity purification (TAP) and protein identification with mass spectrometry (MS) to reveal previously unknown Kv4.2 interactions in hippocampal neurons (Hu et al., 2020b). As expected, Kv4.2 pulled down Kv4.x, DPP, and KChIP auxiliary subunits, confirming the specificity of the assay (Figure 1A). In addition to known interactions, we identified peptides representing the Cav2.3 amino acid sequence (Figures 1A and S1). Cav2.3 was the only ion channel identified in this screen. To confirm that Cav2.3 and Kv4.2 form a complex, we assessed their distributions in area CA1 of the hippocampus. CA1 neuropil colocalization of the Cav2.3 and Kv4.2 immunofluorescent signal was consistent with their reported enrichment in hippocampal dendrites (Figure 1B) (Parajuli et al., 2012; Rhodes et al., 2004). To evaluate Cav2.3-Kv4.2 colocalization in dendrites and spines, we transfected cultured hippocampal neurons with equimolar quantities of Cav2.3-GFP (i), Kv4.2-myc (ii), and mCherry (iii) plasmids (Figure 1C). In addition to co-localization in dendrites, Cav2.3-GFP and Kv4.2-myc were enriched in spines relative to the cytosolic mCherry fluorescent protein (Figures 1D and 1E). To more precisely assess Cav2.3 and Kv4.2 colocalization in spines, we performed double immunogold electron microscopy. Despite the low labeling efficiency of this technique, Cav2.3 and Kv4.2 particles were visible near synapses in spines, and we found evidence of colocalization near the postsynaptic density (Figure 1Fi) and in the spine head (Figures 1Fii and S2). To confirm Cav2.3 and Kv4.2 binding in native tissue, we co-immunoprecipitated Kv4.2 after Cav2.3 pulldown in lysates from wild-type (WT) hippocampus, but not from a previously characterized Cav2.3 knockout (KO) mouse line (Figures 1G and S3) (Gutzmann et al., 2019; Wilson et al., 2000). If Cav2.3 and Kv4.2 physically associate, then we reasoned that assembly would result in a decrease in Cav2.3 and Kv4.2 fluorescence recovery after photobleaching (FRAP) mobile fraction. HEK293-FT cells were transfected with either YFP-Cav2.3 and CFP or Kv4.2-CFP and YFP, and YFP-Cav2.3 and Kv4.2-CFP were photobleached in separate cells (Figure S4A). The YFP-Cav2.3 mobile fraction (66.49% ± 0.01%) was larger than Kv4.2-CFP (56.01% ± 0.09%) (Figures 1H and 1J). To assess the reciprocal regulation of the mobile fraction between Cav2.3 and Kv4.2, YFP-Cav2.3 and Kv4.2-CFP were coexpressed and photobleached simultaneously (Figure S4B). The FRAP mobile fraction decreased for both YFP-Cav2.3 (56.28% ± 0.22%) and Kv4.2-CFP (36.77% ± 0.12%), suggesting that Cav2.3 and Kv4.2 can bind independent of auxiliary subunits (Figures 1I and 1J). We next determined whether Cav2.3 regulates the Kv4.2 mobile fraction in hippocampal neuron dendrites and spines by transfecting WT or Cav2.3

KO mouse neurons with Kv4.2-GFP and mCherry (cell-fill) and photobleaching small (~0.5 mm^3) volumes of dendrite shafts or whole spines (Figures S4C and S4D). Kv4.2-GFP was more mobile in dendrites (55.96% ± 0.01%) than in spines (45.00% ± 0.02%) (Figure 1M), consistent with the spine neck acting as a barrier to diffusion, and reported Kv4.2 interactions with postsynaptic scaffold proteins, including PSD95 (Hammond et al., 2008; Wong et al., 2002), SAP97 (Gardoni et al., 2007), and A-kinase anchoring protein 79/150 (AKAP79/150) (Lin et al., 2011). Kv4.2-GFP mobile fraction was increased specifically in dendrite shafts (9.85% ± 3.21%) as opposed to spines (6.45 ± 3.21%) of Cav2.3 KO mouse neurons (Figures 1K–1M). Our electron microscopy (EM) data suggest that Cav2.3 and Kv4.2 interact in spines, but a high concentration of immobile Kv4.2-binding partners in spines may have interfered with our measurement. FRAP results in both HEK293-FT cells and neurons lend support for a physically coupled Cav2.3-Kv4.2 complex in hippocampal dendrites and excitatory synapses.

Cav2.3 and Kv4.2 bind at a 1:1 channel stoichiometry within a cellular nanodomain

After confirming Cav2.3 and Kv4.2 binding, we next determined whether Cav2.3 and Kv4.2 were within proximity to directly interact. Fluorescence resonance energy transfer (FRET) is a distance-dependent process that involves the non-radiative transfer of energy from an electronically excited donor to a nearby acceptor fluorophore; FRET decays at the inverse sixth power of distance and is detected only when donor and acceptor are <10 nm apart (Förster, 1948; Lakowicz, 2006). To assess Kv4.2 and Cav2.3 proximity, we introduced Kv4.2-CFP (cyan fluorescent protein) or YFP-Cav2.3 into HEK293-FT cells with YFP or CFP, respectively, to rule out spurious FRET (0.68% ± 0.34% and 0.46% ± 0.21%) (Figures 2A and 2B). We then coexpressed Kv4.2-YFP and KChIP3a-CFP, which, as expected, yielded a high FRET efficiency (11.22% ± 0.57%). The coexpression of Kv4.2-CFP and YFP-Cav2.3 resulted in FRET (6.71% ± 0.39%), confirming that they bind within 10 nm (Figures 2A and 2B). Next, we leveraged the maximum FRET signal at either the donor ($FRET_{D,MAX}$) or acceptor ($FRET_{A,MAX}$) using saturating concentrations of free acceptors or donors to determine the stoichiometry of the Cav2.3-Kv4.2 complex (Ben-Johny et al., 2016). The stoichiometry was deduced from the maximal efficiency of interacting acceptors and donors expressed as the stoichiometry ratio ($FRET_{A,MAX}/FRET_{D,MAX}$). We validated this method using known stoichiometries of Kv4.2 to KChIP (1:1) and AKAP79 to the Protein Kinase A regulatory subunit, RIIα (1:2) binding. After coexpressing varying ratios of Kv4.2-YFP and KChIP3a-CFP, we measured similar maximum FRET efficiencies at both donor and acceptor ($FRET_{A,MAX}$: 15.98% ± 0.64%; $FRET_{D,MAX}$: 15.75% ± 0.79%) consistent with a 1:1 interaction (Figures 2C, 2F, and 2G). For AKAP79-YFP and PKA-RII-CFP, we measured maximum FRET efficiencies that were the most consistent with the expected 1:2 stoichiometry ($FRET_{A,MAX}$:13.28% ± 1.13%; $FRET_{D,MAX}$: 5.35% ± 0.26%) (Figures 2D, 2F, and 2G). Determination of the stoichiometry of YFP-Cav2.3 and Kv4.2-CFP indicated that the FRET complex was most consistent with a 1:4 acceptor-to-donor ratio that would be expected for a complex containing a single pore-forming YFP-Cav2.3 α1 subunit and a Kv4.2-CFP homotetrameric channel ($FRET_{A,MAX}$:14.52% ± 1.14%; $FRET_{D,MAX}$: 3.43% ± 0.33%) (Figures 2E–2G). These FRET experiments confirm that binding occurs within 10 nm, a requirement for direct binding, and within the plume of Cav2.3-mediated Ca^{2+} influx

required for Ca^{2+} binding to Kv4.2-KChIP (Augustine et al., 2003; Naraghi and Neher, 1997).

Cav2.3 coexpression increases Kv4.2 current density and surface localization in a KChIP- and Ca^{2+}-dependent manner

We and others have reported an increase in Kv4.x current density when intracellular free Ca^{2+} was increased to the micromolar range (Murphy and Hoffman, 2019; Seifert et al., 2020). Nanoscale Cav2.3-Kv4.2 binding suggests that Cav2.3 could act as a local micromolar source of free Ca^{2+}. To test this, we expressed either Kv4.2 alone (i), Kv4.2 and KChIP2c (ii), or Kv4.2, KChIP2c, and Cav2.3 (iii) in HEK293-FT cells (Figure 3A). As expected, KChIP2c increased Kv4.2 current density and slowed fast inactivation of the macroscopic current (Figures 3B and 3C; Table S1). The coexpression of Cav2.3 further increased Kv4.2 current density (Figures 3B and 3C) without affecting KChIP-mediated regulation of Kv4.2 voltage-dependent inactivation or recovery from inactivation (Figures 3E and 3F). If local Cav2.3-mediated Ca^{2+} influx led to increased Kv4.2 current, then this could be disrupted by replacing EGTA with the fast Ca^{2+} chelator BAPTA to limit Ca^{2+} diffusion. BAPTA blocked Cav2.3-mediated enhancement of Kv4.2 current density (Figures 3B and 3C), consistent with a Cav2.3-mediated Ca^{2+} influx effect. Coexpression of a Ca^{2+}-dead EF-hand mutant KChIP2c also reversed the Cav2.3 effect (Figure 3C). Neuronal I_A, the endogenous Kv4.2 current, requires the coexpression of KChIP and DPPs in heterologous expression systems (Nadal et al., 2003). To demonstrate that Cav2.3 regulation of Kv4.2 occurs in the context of the native complex, we recorded from cells expressing Kv4.2, KChIP2c, and DPP6S. As above, Kv4.2 current density was also BAPTA and KChIP EF-hand mutant sensitive in the presence of DPP6S (Figures S5A and S5B; Table S1). The regulation of Kv4.2 current density by Cav2.3 Ca^{2+} influx could be explained by an increase in Kv4.2 surface localization. To test this possibility, we transfected COS-7 cells with Kv4.2 alone, Kv4.2 and Cav2.3, Kv4.2 and KChIP2c, or Kv4.2, Cav2.3, and KChIP2c. Cav2.3 coexpression led to an increase in surface Kv4.2 biotinylation when compared to KChIP alone (Figures 3G, 3H, S6A, and S6B). Therefore, the assembly of Cav2.3 and Kv4.2 increases Kv4.2 current in a Cav2.3-mediated Ca^{2+} entry and KChIP-dependent manner in a mechanism consistent with increased surface localization.

Cav2.3 regulates I_A and Kv4.2 surface localization in cultured hippocampal neurons

After establishing functional regulation of Kv4.2 by Cav2.3 in HEK293-FT cells, we next tested Cav2.3 regulation of native neuronal I_A. We found that the peak outward K^+ current in was enriched for I_A relative to the sustained current (92.49% ± 0.02%) in 6–8 days *in vitro* (DIV 6–8) hippocampal neurons (Figures S7A–S7D). This was consistent with Kv4.2 staining the developing rat hippocampus (Maletic-Savatic et al., 1995). Therefore, we monitored total peak outward current as a proxy for I_A. Voltage clamp recordings were stable over a 360 s recording period (Figures 4Ai, 4B, and 4C). We confirmed the contribution of Kv4.x-containing channels to I_A using 500 nM AmmTx3, a Kv4.x selective toxin (Figures 4Aiii, 4B, and 4C) (Maffie et al., 2013; Vacher et al., 2002). A concentration that selectively blocks Cav2.3, 200 mM Ni^{2+}, was used as an alternative to the toxin SNX-482 that has been reported to potently inhibit Kv4.x channels (Kimm and Bean, 2014). The application of Ni^{2+} led to a rapid and sustained reduction in I_A (Figures 4Aii, 4B, and

4C). Ni^{2+} regulation of I_A was dose dependent and the apparent half-maximal inhibitory concentration (IC_{50}) (~44.1 μM) approximated values reported for Cav2.3 (27.4–66.0 μM) (Figure S8A) (Williams et al., 1994). Ni^{2+} did not affect voltage dependence of inactivation for I_A, suggesting a distinct mechanism in hippocampus relative to cerebellum (Figure S8B) (Anderson et al., 2010). To determine whether the Ni^{2+} block of Cav2.3 channels mediated a reduction in surface Kv4.2 channels as in HEK293-FT cells, we performed Kv4.2 surface biotinylation in DIV 7 hippocampal neurons treated with 200 μM Ni^{2+}. We detected a reduction in Kv4.2 surface expression in treated neurons when compared to untreated controls (Figures 4D, S9A, and S9B). At 200 μM Ni^{2+}, Cav3.x channels were likely also blocked. To address any role for Cav3.x, we used a Cav3.x-selective concentration of 50 μM Ni^{2+} and a Cav3.x-specific blocker (5 μM TTA-P2). We found that surface Kv4.2 levels were not regulated by Cav3.x channels (Figures 4D and S9C). To determine whether the effects of 200 μM Ni^{2+} on I_A were specific to Cav2.3 R-type currents, we recorded whole-cell I_A using selective antagonists of all of the known neuronal voltage-gated calcium channels (VGCCs). Blockers for Cav3.x (5 μM TTA-P2), Cav1.x (5 μM nimodipine), and Cav2.1/Cav2.2 (1 μM ω-conotoxin GVIA +3 μM ω-conotoxin MVIIC) did not reduce whole-cell I_A (Figure 4E). Furthermore, Ni^{2+} led to a greater reduction in whole-cell I_A in WT compared to Cav2.3 KO neurons (72.11% ± 0.04% versus 81.51% ± 0.01%, p = 0.049). Ni^{2+} block of Cav2.3 channels acutely regulates Kv4.2 function, at least in part, through a surface localization-mediated mechanism in hippocampal neurons.

Disruption of the I_A gradient in Cav2.3 KO CA1 pyramidal neuron dendrites

Kv4.2 channels in CA1 neurons regulate active processes in dendrites to transform synaptic input and set the threshold for synaptic plasticity. Therefore, we wanted to determine the state of I_A in CA1 dendrites of Cav2.3 KO mice. Somatic I_A was reduced in whole-cell recordings from Cav2.3 KOs when compared to WT (Figure 5A). This could be explained by a reduction in I_A-conducting channels at the somatic cell membrane. However, somatic outside-out patches did not replicate the whole-cell reduction in I_A (Figure 5B). We next asked whether the whole-cell reduction in I_A observed in Cav2.3 KO recordings arose from a specific loss of dendritic Kv4.2 channels. To determine this, we performed cell-attached recordings along the apical dendrite. Comparison of distal versus proximal I_A suggested that the reduced I_A measured at the soma was due to a reduction in dendritic I_A-conducting channels in Cav2.3 KO neurons (Figure 5C). Kv4.2 subunits have been reported to conduct the majority of I_A in hippocampal pyramidal neuron dendrites (Chen et al., 2006b). To determine whether the loss of I_A was due to a reduction in dendritic Kv4.2 subunits, we measured Kv4.2 expression in the stratum radiatum (SR) of hippocampus area CA1. We found a significant reduction in Kv4.2 expression in Cav2.3 KO mouse hippocampal SR when compared to WT (Cav2.3 KO: 89.23% ± 0.034%; WT: 100% ± 0.027%; p = 0.029) (Figures 5D and S10). Kv4.2 expression in the principal cell layer of area CA1 was equal in WT and Cav2.3 KO mice (Cav2.3 KO: 93.95% ± 0.063%; WT: 100% ± 0.049%; p = 0.465) (Figures 5D and S10). These results suggest that Cav2.3 channel expression regulates the characteristic graded expression of Kv4.2-mediated I_A in dendrites.

Cav2.3 promotes I_A-mediated attenuation of spontaneous synaptic currents

Voltage-gated ion channels open in response to glutamate receptor-mediated depolarization of synapses (Magee et al., 1995; Bloodgood and Sabatini, 2007; Seong et al., 2014; Grunditz et al., 2008). As a consequence, the amplitude of the synaptic current measured at the cell soma represents the integration of glutamate receptor and voltage-activated membrane conductances. Kv4.2 and Cav2.3 channels are localized to CA1 spines and dendrites where they independently shape the synaptic potential and regulate its propagation (Bloodgood and Sabatini, 2007; Bloodgood et al., 2009; Hoffman et al., 1997; Kerti et al., 2012; Parajuli et al., 2012; Wang et al., 2014, 2015). We and others have previously shown that I_A reduces the magnitude of spontaneous miniature excitatory postsynaptic currents (mEPSCs) (Kim et al., 2007; Wang et al., 2014). Therefore, if Cav2.3 channels boost I_A, Ni^{2+}-mediated reduction of I_A could enhance mEPSCs. To test this, we applied Ni^{2+} and recorded spontaneous mEPSCs at a holding potential of −70 mV (Figure 6A). Ni^{2+} produced a rightward shift in the distribution of mEPSC amplitudes, but with reduced effect when compared to blockade of Kv4.2 with AmmTx3 (Figure 6B). Ni^{2+} and AmmTx3 together mimicked AmmTx3 alone, suggesting that AmmTx3-mediated Kv4.2 channel block occluded the Ni^{2+} effect without synergism (Figures 6B and 6C). Despite an increase in mEPSC amplitude, Ni^{2+} reduced mEPSC frequency. This may suggest a presynaptic effect of Ni^{2+} on VGCCs that contribute to neurotransmitter release in the hippocampus; however, this was not observed in Cav2.3 KO mice (Figure 6C). To assess whether Cav2.3 expression was involved in Kv4.2 regulation of spontaneous synaptic events, we measured the AmmTx3-sensitive fraction of mEPSCs in WT or Cav2.3 KO mouse neurons. The amplitudes of mEPSCs recorded from WT neurons treated with AmmTx3 were greater than those of untreated controls (Figures 6D–6F). Consistent with reduced Kv4.2 synaptic function, AmmTx3 did not increase mEPSC amplitudes in Cav2.3 KO mouse neurons (Figures 6G–6I). The above results support a role for Cav2.3 as an integral component of Kv4.2 channel complexes required for the regulation of synaptic input.

Cav2.3 promotes I_A-mediated attenuation of spontaneous quantal spine Ca^{2+} signals

If the Cav2.3-Kv4.2 complex regulates synaptic currents recorded at the cell soma as shown above and by Wang et al. (2014), then it is possible that quantal spontaneous currents in spines may be similarly affected. Fluorescent Ca^{2+} indicators are suited for the visualization of NMDA receptor (NMDAR)-mediated Ca^{2+} entry in response to spontaneous quantal glutamate release events (Murthy et al., 2000; Reese and Kavalali, 2015). We transfected neurons with the fluorescent Ca^{2+} indicator GCaMP6f and mCherry as a cell-filling marker. The frequency, amplitude, and duration of NMDAR-mediated Ca^{2+} signals were highly variable both among and within individual spines (Figure 7A). The NMDAR blocker AP5 abolished Ca^{2+} signals consistent with a requirement for NMDARs Ca^{2+} influx (Figures 7A and 7B). AmmTx3 block of Kv4.2 channels did not affect the amplitude of Ca^{2+} signals, but it did lengthen the event half-width, suggesting that Kv4.2 channels oppose spine depolarization initiated by glutamate receptors (Figure 7C). Kv4.2 block increased the integrated amount of Ca^{2+} entry (Figure 7D). As expected, Ni^{2+} reduced integrated spine Ca^{2+} signals possibly due to a combinatorial effect on Ni^{2+} sensitive pre- and postsynaptic VGCCs (Figure 7E). To determine whether Cav2.3 Ca^{2+} entry was required for the regulation of spine depolarization by Kv4.2 channels, we pre-applied Ni^{2+} to block

Cav2.3 and determined the remaining AmmTx3-sensitive Kv4.2-mediated component of the spine Ca^{2+} signal. Preapplication of Ni^{2+} occluded the AmmTx3-sensitive increase in spine Ca^{2+}, suggesting that Cav2.3 channels are required to maintain the Kv4.2 regulation of spine repolarization (Figure 7F). Unlike WT mouse neurons, we found that quantal spine Ca^{2+} signals were not amplified in Cav2.3 KO mouse neurons treated with AmmTx3 (Figures 7G and 7H). The loss of Kv4.2 regulation led to larger basal spine Ca^{2+} signals in Cav2.3 KO neurons when compared to WT (Figure 7I). As a consequence, Cav2.3 function and expression were required for the Kv4.2-mediated regulation of spontaneous quantal spine Ca^{2+} events.

DISCUSSION

The present study was designed to confirm and define the nature of a Cav2.3-Kv4.2 complex identified in a proteomic screen and to assess its functional role in hippocampal pyramidal neurons. We showed that Cav2.3 and Kv4.2 colocalize at 1:1 stoichiometry and within dendritic spine nanodomains independent of auxiliary subunits (Figures 1 and 2). Functionally, we found that the Cav2.3-Kv4.2 interaction increases Kv4.2 surface localization and contributes to the maintenance of the I_A dendritic gradient (Figures 3, 4, and 5). Previous studies have demonstrated that dendritic I_A regulates excitability, spine Ca^{2+} entry, action potential back propagation, plateau potentials, synaptic plasticity, and hippocampus-dependent learning (Shah et al., 2010; Stuart et al., 2016; Johnston et al., 2003). By regulating the magnitude of I_A, the Cav2.3-Kv4.2 complex therefore plays a fundamental role in dendritic function. Cav2.3-mediated Ca^{2+} entry likely promotes the reported roles for dendritic I_A. We found that Cav2.3 channels are required for AmmTx3-mediated boosting of mEPSCs and spine Ca^{2+} signals (Figures 6 and 7).

The close proximity of the Cav2.3-Kv4.2 interaction is likely critical for the concerted regulation of synaptic input by the ion channel complex. A recently reported cryo-EM structure measured the diameter of the Kv4.2-KChIP complex at ~14.5 nm (Kise et al., 2021). The distance dependence of FRET (<10 nm) suggests that Cav2.3 and Kv4.2 may bind directly. Therefore, KChIPs arrayed around the intracellular domains of Kv4.2 could be exposed to Ca^{2+} concentrations approaching 10 μM during Cav2.3 channel openings based on Ca^{2+} source diffusion models (Augustine et al., 2003). While the *in vivo* Ca^{2+} occupancy of KChIP is unknown, dynamic Ca^{2+} binding may account for Cav2.3-mediated regulation of Kv4.2 surface expression through reduced channel turnover. In a test tube, Ca^{2+} binds to KChIP at high- (EF3 and EF4) and low-affinity sites (EF2), and Ca^{2+} binding promotes KChIP folding and binding to Kv4.x channels (Craig et al., 2002; Osawa et al., 2001; Pioletti et al., 2006). While these studies are informative, an *in vivo* mechanism to explain how dynamic KChIP-Ca^{2+} exchange may regulate Kv4.x function remains elusive. In the present study, we report measurements of I_A in cultured neurons and hippocampal slices to provide evidence for Cav2.3 regulation of the magnitude of I_A (Figures 4 and 5). Cav2.3-mediated Ca^{2+} entry was required to increase Kv4.2 functional expression in a KChIP-dependent manner in non-neuronal cells (Figure 3). Several lines of evidence support a Cav2.3-mediated Ca^{2+}- and KChIP-dependent surface expression mechanism as opposed to the regulation of Kv4.2 conductance or gating in CA1 pyramidal neurons. First, while previous studies have ruled out increased single-channel conductance as a mechanism for

the increase in Kv4.2 current density mediated by KChIPs (Beck et al., 2002; Holmqvist et al., 2002), it has yet to be determined whether the elevations of intracellular Ca^{2+} may regulate Kv4.2 single-channel conductance. Second, we previously reported that elevated intracellular Ca^{2+} led to an increase in Kv4.x current density without affecting classical KChIP-dependent processes, including inactivation gating (Murphy and Hoffman, 2019). However, the stoichiometry of KChIP binding is expression dependent (Kunjilwar et al., 2013; Kitazawa et al., 2014) and a Ca^{2+} induced shift in Kv4.x-KChIP binding affinity may be overcome by the 8 KChIP to 1 Kv4.x plasmid DNA molar stoichiometry used in those studies. Lastly, we found increased Kv4.2 surface localization by Cav2.3 coexpression in HEK293-FT cells (Figures 3G and 3H), an acute Ni^{2+}-mediated decrease in surface Kv4.2 in hippocampal neurons (Figure 4D), and a reduced dendritic expression of Kv4.2 subunits in CA1 SR micro-dissections of Cav2.3 KO mice (Figure 5D). Cav2.3 and Kv4.2 functional coupling in hippocampal neurons increases the Kv4.2 current amplitude through enhanced surface expression or stability. Therefore, reduced surface localization of Kv4.2 channels may explain the reported EPSP boosting by Cav2.3 block (Wang et al., 2014). This contrasts with the mechanism reported for the cerebellar Cav3.x-Kv4.x complex that promotes I_A via a shift in channel availability to more negative potentials (Anderson et al., 2010). It remains to be determined what mediates the disparate regulatory mechanisms in the hippocampus and cerebellum. We demonstrated the specificity of Cav2.3 regulation of neuronal I_A in the hippocampus using VGCC pharmacology and Cav2.3 KO mice (Figure 4E). Our observation of residual whole-cell I_A regulation by Ni^{2+} treatment in DIV 6–9 Cav2.3 KO neurons, although less so than in WT, suggests that there may be compensatory mechanisms to maintain I_A in the absence of Cav2.3 expression (Figures 4F and 4G). Perhaps other VGCC subtypes may be able to regulate Kv4.x channels in the absence of Cav2.3, particularly in immature neurons. Importantly, compensation did not salvage the dendritic I_A gradient nor loss of I_A-mediated attenuation of synaptic input in Cav2.3 KO adult mouse hippocampal neurons (Figures 5, 6, and 7).

In the present report, we have described voltage-gated channel-mediated regulation of quantal NMDAR-mediated Ca^{2+} signals (Figure 7). In prior studies, pharmacological block of either AMPAR or voltage-gated channels had no measurable effect on quantal NMDAR-mediated Ca^{2+} transients (Metzbower et al., 2019; Walker et al., 2017). However, subthreshold synaptic depolarizations can activate voltage-gated channels including R-type (Cav2.3), T-type (Cav3.x), and A-type (Kv4.x) channels, all of which are activated at relatively hyperpolarized membrane potentials (Bloodgood and Sabatini, 2007; Grunditz et al., 2008; Hoffman et al., 1997; Magee et al., 1995; Seong et al., 2014). Why did prior studies not find a contribution of voltage-gated channels to the quantal NMDAR-mediated Ca^{2+} signals? The Ca^{2+} signal variability between spines necessitated our more straightforward approach of within-spine comparisons. We also found that AmmTx3 regulated the duration of spine Ca^{2+} events more so than amplitude, leading us to compare Ca^{2+} signal integrals. Kv4.2 regulation of NMDAR Ca^{2+} signals were consistent with the known role of Kv4.2 channels in synaptic plasticity and implicates Cav2.3 as a critical component of an ion channel complex that regulates NMDAR-mediated synaptic signaling.

I_A increases linearly ~5-fold on the distal apical dendrites 350 mm from the soma of rat CA1 pyramidal neurons (Hoffman et al., 1997). Curiously, histochemical measurements of Kv4.2

expression levels suggest at most a 2-fold increase in expression along the proximal-distal extent of the SR (Kerti et al., 2012; Maletic-Savatic et al., 1995; Rhodes et al., 2004; Varga et al., 2000). A constellation of studies supports that both auxiliary subunit and enzyme-dependent pathways may underlie the disparity between Kv4.2 expression and function. The DPP6 auxiliary subunit establishes the Kv4.2 functional gradient in CA1 pyramidal neurons through enhanced dendrite-directed surface expression and increased availability of Kv4.2 at hyperpolarized membrane potentials, particularly in distal dendrites (Hoffman et al., 1997; Sun et al., 2011). The increased availability of distal dendritic I_A was reversed by protein kinase A (PKA), PKC, or mitogen-activated ki-nase pathways (Hoffman and Johnston, 1998; Yuan et al., 2002; Watanabe et al., 2002). Strong synaptic stimulation promoted Kv4.2 internalization in an NMDAR- and Ca^{2+}-dependent manner by PKA phosphorylation at S522 (Kim et al., 2007; Hammond et al., 2008). Furthermore, Kv4.2 surface expression was bidirectionally regulated by local signaling of the Ca^{2+}—activated phosphatase calcineurin (CaN) and PKA through the postsynaptic scaffolding protein AKAP79/150 (Lin et al., 2011). Another Ca^{2+}-dependent enzyme, Ca^{2+}/calmodulin-dependent kinase II, has also been shown to promote Kv4.2 surface expression through direct C-terminal phosphorylation of S438 and S459 (Varga et al., 2004). We recently reported that the proline isomerase Pin1 regulates activity-dependent downregulation of Kv4.2 through p38 phosphorylation of T607 (Hu et al., 2020a, 2020b). Thus, differential localization of kinases and phosphatases along the proximal-distal axis of CA1 pyramidal neurons could underlie the I_A gradient. It is possible that Cav2.3 Ca^{2+} entry may impinge on these pathways in a Ca^{2+}-nanodomain fashion. For example, AKAP79/150 localizes PKA and CaN for phosphoregulation of AMPAR and L-type Ca^{2+} channels (Patriarchi et al., 2018). Hypothetically, Cav2.3 Ca^{2+} entry could also drive the activation of A kinase anchoring protein (AKAP)-anchored CaN and dephosphorylate Kv4.2 channels, favoring surface expression. Deciphering the mechanistic link between local Ca^{2+} influx and increased Kv4.2 surface expression is a goal for future research.

KChIP heterogeneity is a largely unexplored area of research in CA1 pyramidal neurons. Alternative splicing and variable start sites of the *KCNIP1–4* transcripts result in over a dozen possible KChIP isoforms. KChIP1–4 variants have been categorized based on membrane interactions of alternative N termini (Jerng and Pfaffinger, 2014). A subset of “cytoplasmic” KChIP isoforms confer Ca^{2+} regulation onto Kv4.2 channel complexes, *N*-myris-toylated isoforms do not, and reversibly palmitoylated isoforms have mixed Ca^{2+} sensitivity (Murphy and Hoffman, 2019). Members of a fourth transmembrane class of KChIPs retain Kv4.2 complexes within the endoplasmic reticulum (ER) and reduce Kv4.2 surface expression when compared with other KChIP isoforms (Jerng and Pfaffinger, 2008). In the hippocampus, there is overlapping expression of both Ca^{2+}-sensitive and Ca^{2+}-insensitive KChIP isoforms. Could differential subcellular targeting of KChIPs lead to increased Kv4.2 function in distal dendrites? Perhaps membrane-localized KChIPs, such as the Kv4.2 suppressor KChIP4a, may be restricted to soma and proximal dendrites. *KCNIP1–4* mRNAs have been detected in the CA1 neuropil, suggesting that they may be locally translated (Biever et al., 2020; Cajigas et al., 2012). Dendrite-targeted *KCNIP* mRNAs may also undergo alternative splicing for conditional or spatiotemporal modification of Kv4.2 function. In fact, a KChIP4bL- to-KChIP4a splicing shift occurs in postmortem brain tissue

isolated from patients with Alzheimer's disease, that would be predicted to result in reduced functional I_A (Massone et al., 2011). KChIPs may also confer Ca^{2+} regulation to Kv4.x complexes through mechanisms unrelated to direct KChIP-Ca^{2+} binding. KChIP and DPP assembly with Kv4.2 promotes S552 phosphorylation and surface expression, and their coexpression is also required for the downregulation of Kv4.2 surface expression in response to PKA Ser552 phosphorylation (Schrader et al., 2002; Seikel and Trimmer, 2009; Shibata et al., 2003). In addition, reduced Kv4.x function by arachidonic acid was mediated by assembly with KChIPs (Holmqvist et al., 2001). Thus, ultrastructural roles of KChIPs may augment Kv4.2 function by affecting sensitivity to some forms of regulation.

The majority of CA1 dendritic I_A is mediated by Kv4.2 subunits, ruling out a significant contribution of other A-type channels that include Kv1.4, Kv3.4, and Kv4.x subtypes (Chen et al., 2006b). Here, we show that the I_A gradient in dendrites was disrupted in the Cav2.3 KO mouse (Figure 5C). Others have shown that Ni^{2+}-sensitive VGCCs are a source of Ca^{2+} in dendrites and spines (Bloodgood and Sabatini, 2007; Grunditz et al., 2008; Magee et al., 1995; Seong et al., 2014). Given our results, might tonic Cav2.3 activity in distal dendrites sustain Kv4.2 functional expression? The dendritic gradient of Kv4.2 expression correlates with the ratio of excitatory and inhibitory synapses along the apical dendrite layers of the hippocampus (Megias et al., 2001; Nicholson et al., 2006). Therefore, ongoing spontaneous excitatory synaptic transmission and Cav2.3 activity may maintain Kv4.2 expression as a homeostatic mechanism to regulate local dendritic excitability. Long-term potentiation (LTP) of synaptic inputs may override this by stimulated endocytosis of Kv4.2 in an NMDAR-dependent mechanism as we have previously described (Hammond et al., 2008; Kim et al., 2007). This would comport with the increased excitability of dendritic segments containing potentiated synapses following Shaffer collateral-CA1 LTP (Johnston et al., 2003). Our findings suggest several avenues of research into the function of the Cav2.3-Kv4.2 complex in dendrite function; however, a lack of Cav2.3-specific pharmacology without overlapping effects at Kv4.x channels makes this work challenging. Future studies aimed toward identifying Cav2.3-Kv4.2 interaction domains could be leveraged to disrupt the complex and determine roles specific to the Cav2.3-Kv4.2 interaction.

Limitations of the study

In the course of research, study design and interpretation of the findings are influenced by their inherent limitations. In the work presented above, we detected an increase in AMPAR-mediated mEPSC amplitude in response to the AmmTx3 blockade of Kv4 channels. It should be noted that in the whole-cell voltage clamp configuration (−70 mV), there is limited voltage control over the measured synaptic responses (Beaulieu-Laroche and Harnett, 2018). Under these conditions, AmmTx3 block of Kv4 channels may alter the resting membrane voltage and reduce the driving force for AMPAR-mediated Na^+ entry. However, we found that Kv4 block led to an increase in the measured mEPSC amplitude, suggesting that Kv4 channels attenuate synaptic responses as previously shown (Kim et al., 2007; Wang et al., 2014). Kv4-mediated currents, elicited by glutamatergic synaptic depolarizations in unclamped spines, may also directly counteract the measured AMPAR-mediated mEPSCs. To address whether Kv4 channels regulate the magnitude of synaptic responses in a more direct manner, we made optical measurements of spontaneous

NMDAR-mediated Ca^{2+} influx in dendritic spines. These measurements were consistent with our mEPSC findings that Cav2.3 channels promote Kv4-mediated attenuation of synaptic responses, but without the caveats intrinsic to whole-cell voltage clamp recordings of synaptic physiology.

STAR★METHODS

RESOURCE AVAILABILITY

Lead contact—Further information and requests for resources and reagents should be directed to and will be fulfilled by the lead contact, Jonathan Murphy (Jonathan.murphy@nih.gov).

Materials availability—All plasmids generated in this study are available upon request.

Data and code availability

- All original western blots images, electron and fluorescence microscopy, and electrophysiological data will be shared by thelead contact upon request.
- This paper does not report original code.
- Any additional data required to reanalyze the data reported in this paper is available from the lead contact upon request.

EXPERIMENTAL MODEL AND SUBJECT DETAILS

Animals—All protocols and procedures were approved by the *Eunice Kennedy Shriver* National Institute of Child Health and Human Development Animal Care and Use Committee. All mice were group housed and bred in the Porter Neuroscience Research Center animal facility at the National Institutes of Health in Bethesda, MD. Rodents were maintained on a 12 h light/dark cycle with *ad libitum* access to rodent chow and water. All animals were experimentally naïve prior to use. Cav2.3 KO mice used for hippocampal cultures and brain slice electrophysiology were generously provided by Dr. Richard Miller, Northwestern University (Wilson et al., 2000). Cav2.3 KOs were backcrossed and maintained on a C57BL/6J background. Age-matched wild-type C57BL/6J mice (WT) (Jackson Labs; Cat#0006664; RRID: IMSR_JAX:000664) were used as controls. Rat hippocampal neuronal cultures were prepared with embryos collected from E18–19 timed pregnant Sprague Dawley rats bred at Taconic Biosciences and housed at the NIH for 4–5 days prior to euthanasia.

Cell lines—HEK293-FT (female) (ThermoFisher; R70007; RRID: CVCL_6911) and COS-7 cells (Male) (ATCC; CRL-1651; RRID: CVCL_0224) were maintained in DMEM supplemented with 10% fetal bovine serum (ThermoFisher, A3160501) and 2% penicillin/streptomycin (ThermoFisher, 15140122) at 37°C and 5.0% CO_2. Cells were passaged 2x weekly by seeding 0.5–1.0 × 10^6 cells into 10 cm culture dishes (Corning). Cell lines were not subjected to cell authentication. Cell lines were limited to 20 passages.

METHOD DETAILS

Mammalian expression vectors—Cav2.3-GFP was a gift from Ehud Isacoff, University of California Berkeley (Ulbrich and Isacoff, 2007). The SGFP2-N1 plasmid was generated by replacement of YFP in YFP-N1 using AgeI/BsrGI sites to excise SGFP2 from pSGFP2-C1 (Dorus Gadella, Addgene 22881). Kv4.2-CFP, Kv4.2-YFP, and Kv4.2-SGFP2 fusions were created by ligating the mouse Kv4.2 (CCDS: 29974.1) from Kv4.2-GFP (Kim et al., 2007) into the CFP-N1 vector using SalI/BglII sites. YFP-Cav2.3 was generated by PCR amplification of the human Cav2.3 (CCDS: 55664.1) coding sequence from Cav2.3-GFP using BglII/HindIII sites for ligation into the YFP-C1 vector (performed by Bioinnovatise, Inc). Mouse pcDNA3.DPP6S was a gift from Bernardo Rudy. Rat pCMV-KChIP2c was a gift from Henry Jerng and Paul Pfaffinger, Baylor College of Medicine, Houston, TX. Ca^{2+}-dead KChIP2c was generated by site directed mutagenesis using D->A mutations at position 1 of each of EF2,3, and 4 (Stratagene, QuikChange Site-Directed Mutagenesis Kit). KChIP2c-CFP was generated by PCR amplification of the rat KChIP2c ORF (GenBank: NM_001033961.1) from pCMV-KChIP2c and subcloned into CFP-N1 using BglII/SalI sites. AKAP79-YFP and PKARII-CFP were gifts from Mark L. Dell'Acqua, University of Colorado School of Medicine, Aurora, CO. The CFP-18aa-YFP tandem fusion construct used for FRET efficiency calibrations was a gift from Clemens Kaminski (University of Cambridge). GCaMP6f was a gift from Douglas Kim & GENIE Project (Addgene 40755). Human Kv4.2-Myc-DDK (Origene, RC215266), ECFP-N1, EYFP-C1, EYFP-N1, and mCherry-N1 are commercially available (Takara Bio).

Antibodies—*Guinea pig anti-Cav2.3* was a generous gift from Akos Kulik, University of Freiburg (Parajuli et al., 2012), 1:100 for EM; 1:1000 for IHC; 1:5000 for WB. *Mouse anti-Cav2.3*: Synaptic Systems 152–441, 1:2000 for WB. *Mouse anti-Kv4.2* (K57/1): NeuroMab 75–016, 1:25 for EM; 1:300 for IHC; 1:2000 for WB. *Mouse anti-Myc*, Millipore 05–419, 1:500 for ICC. *Alexa Fluor 488 goat anti-guinea pig*: ThermoFisher A11073, 1:800 for IHC. *Alexa Fluor 488 goat anti-rabbit*: ThermoFisher A11008, 1:500 for ICC. *Alexa Fluor 555 goat anti-mouse*: ThermoFisher A21422, 1:800 for IHC. *Alexa Fluor 647 goat anti-mouse*: ThermoFisher A21236, 1:500 for ICC. *Alexa Fluor 680 goat anti-mouse*: ThermoFisher A21057, 1:10,000 for WB. *IRDye 800CW goat anti-rabbit*: Li-Cor Biosciences 926–32211, 1:5,000 for WB. *Rabbit anti-GFP*, ThermoFisher A11122, 1:500 for ICC; 1:3000 for WB

Primary culture of rodent hippocampal neurons

Neuronal hippocampal cultures prepared from embryonic day 18–19 (E18) rodent embryos were performed as reported previously (Gray et al., 2019). Female dams were euthanized using CO_2 asphyxiation followed by guillotine decapitation. Embryos were rapidly dissected from the uterine horn, decapitated with sharp scissors, and whole heads were placed in ice-cold dissection medium (ThermoFisher, 1X HBSS (14185052), 1 mM sodium pyruvate (11360070), 10 mM HEPES (15630080), and 30 mM Glucose). After peeling away overlying skin and bone with forceps, brains were removed from the skull and placed into fresh dissection medium. Each hemisphere of the cerebral cortex was bisected from the hindbrain and the hippocampus was then gently rolled away and excised from the cerebral cortex and placed into fresh ice-cold dissection medium. Once all tissue was collected, the dissection medium was replaced with 5 ml room temperature (RT) papain solution (5 ml

dissection solution w/1% DNase (Worthington, LK003170) and 1 vial 0.22 mm filtered Papain (Worthington, LK003176). After a 45 min RT incubation, tissue was washed 43 with prewarmed NB5 medium (5% FBS (Hyclone, SH30071.03), ThermoFisher: 1X Neurobasal A (21103049), 2% Glutamax (35050061), and 2% B27 (17504044). Tissue was dissociated by gentle trituration using a 5 ml plastic serological pipette, cells were filtered through a 70 mm cell strainer (Corning, 352350) and pelleted at 1,000 rpm in a swinging bucket centrifuge (Beckman Coulter Allegra™ 6R) for 5 min at RT. Cells were resuspended in 10 ml NB5, diluted 1:1 in 0.4% Trypan Blue Stain (ThermoFisher, 15250061) and counted with a hemocytometer. Neurons were plated 125,000 (rat) or 175,000 (mouse)/well in a 12–well plate (Corning) containing glass coverslips. 12 mm round Poly-D-lysine/laminin pre-coated glass coverslips (Corning, 354087) were used for electrophysiology. For immunostaining and fluorescence microscopy neurons were plated on in-house Poly-D-lysine/laminin coated 18 mm German glass coverslips (Carolina Biological, 633013). Briefly, UV-sterilized coverslips were incubated overnight in poly-D-lysine (Sigma, P7280–5MG) dissolved in 22 mm filter-sterilized borate buffer (50 mM boric acid, 12.5 mM sodium borate, pH 8.5). The following day, coverslips were washed using sterile water and coated with 0.01 mg/ml mouse Laminin (ThermoFisher, 23017015) in PBS for 3 hrs. 24 hrs after seeding, NB5 was replaced with Neurobasal A (Invitrogen) supplemented as above but without FBS and 1% Glutamax (NB0). Neurons were fed twice per week thereafter by replacing 0.4 ml with 0.5 ml fresh NB0 per well.

Tandem affinity purification-mass spectrometry—TAP-MS was performed as previously described (Hu et al., 2020b). Briefly, TAP-tagged Kv4.2 was subcloned into the lentivirus vector to generate TAP-Kv4.2-IRES-GFP Lentivirus. Dispersed cultured rat hippocampal neurons were infected by TAP-Kv4.2-IRES-GFP Lentivirus or IRES-GFP control Lentivirus on DIV 0 and harvested at DIV14. TAP-Kv4.2 was purified using the TAP purification kit from Agilent (#240107) with some modifications and samples were run on 10% SDS-PAGE gel (Novex/Invitrogen). High and low molecular weight gel fragments were sent to the Taplin Mass Spectrometry Facility at Harvard University for in-gel tryptic digestion and MS analysis.

Double immunogold electron microscopy—Animals used for postembedding, double-immunogold localization were prepared as described previously (Petralia and Wang, 2021). Briefly, two male, adult Sprague Dawley rats were perfused with phosphate buffer, followed by perfusion with 4% paraformaldehyde + 0.5% glutaraldehyde in phosphate buffer, and then the brains were vibratomed, cryoprotected in glycerol overnight, frozen in a Leica EM CPC (Vienna, Austria), and embedded in Lowicryl HM-20 resin in a Leica AFS freeze-substitution instrument. Thin sections were incubated in 0.1% sodium borohydride + 50 mM glycine in Tris-buffered saline plus 0.1% Triton X-100 (TBST), then in 10% normal goat serum (NGS) in TBST, and then with 2 primary antibodies together in 1% NGS/TBST (overnight); then they were incubated with the 2 immunogold-conjugated secondary antibodies (5+15 nm; Ted Pella, Redding, CA, USA) in 1% NGS in TBST with 0.5% polyethylene glycol (20,000 MW) and stained with uranyl acetate and lead citrate. Controls on sections from the same two rats, labeled with the 2 secondary antibodies but without the primary antibodies, showed only rare gold and no colocalization.

Native hippocampal co-immunoprecipitations—For each co-IP experiment (repeated 3 times), two 8–12-week-old wild type C57BL/6 or control Cav2.3-KO mice were used. Both whole contralateral hippocampi (35–40 mg) were dissected from each mouse and collected in lysis buffer: 150 mM NaCl, 20 mM Tris-HCl, 1% CHAPS and protease inhibitor mixture (Roche, USA). Tissue was minced with scissors and incubated on ice for 20 min followed by two rounds of sonication, each consisting of 10 repetitions of 1 s pulses at 30% power. Lysates were rotated for 1 h at 4°C and then centrifuged at 15,000 × g for 20 min at 4°C. Supernatants were rotated at 4°C overnight with either 4 mg anti-Cav2.3 or guinea-pig IgG (ThermoFisher Scientific) as nonspecific control. The antibody-antigen complex was adsorbed onto 50 μl of immobilized protein A (ThermoFisher Scientific) and rotated for 2 h at 4°C. The protein-bead mixtures were washed 7× with lysis buffer containing protease inhibitors. The beads were resuspended in SDS sample buffer (ThermoFisher, NP0007), incubated for 20 min at RT, and immunoblotted as described below.

Cell surface biotinylation—Biotinylation assays were performed as previously described (Kim et al., 2007). COS-7 cells are our preferred cell line for surface biotinylation because of a higher surface to volume ratio and slower dividing time relative to HEK293-FT cells. COS-7 cells were transfected with Kv4.2 and Cav2.3-GFP constructs using X-tremegene 9 transfection reagent (Sigma-Aldrich, 06365779001) for 24–36 h; Cultured hippocampal neurons were plated at 3×10^6 cells per 10 cm dish for each experimental condition. At DIV 7, neuronal culture medium was replaced with ACSF containing 0.5 μM TTX and incubated for 10 min at 37°C. Neurons were then either treated with 50/200 μM Nickel or 5 μM TTA-P2. For controls, the medium was replaced with fresh ACSF for 10 min. Both COS-7 cells and neurons were then rinsed with ice-cold PBS, and surface protein was biotinylated with 1.5 mg/ml sulfo-NHS-SS-biotin reagent (ThermoFisher) in PBS for 30 min on ice. Unbound biotin was quenched with cold 50 mM glycine in PBS. Cells were lysed with ice-cold lysis buffer: 150 mM NaCl, 20 mM Tris-HCl, 1% CHAPS and protease inhibitor mixture (Roche Diagnostics), sonicated and centrifuged at 12,000 g for 10 min. Cell lysates were incubated overnight at 4°C with immobilized-Streptavidin agarose beads (ThermoFisher), and unbound protein was removed from the beads with 5 washes in lysis buffer. The bound proteins were eluted with SDS sample buffer (ThermoFisher, NP0007). Surface fractions and whole cell lysates were immunoblotted as described below.

Hippocampal CA1 micro-dissection—Whole brains were dissected from deeply anaesthetized 6 to 8-week-old WT and Cav2.3 KO mice and immediately transferred into ice-cold slicing solution containing in mM: 2.5 KCl, 28 $NaHCO_3$, 1.25 NaH_2PO_4, 7 Glucose, 0.5 $CaCl_2$, 7 $MgCl_2$, 233 Sucrose, and bubbled with 95% O_2 / 5% CO_2. Using a Leica VT1200S vibrating microtome, 300 mm coronal hippocampal slices were transferred to a glass surface on dry ice. Aided by a dissection microscope, either the CA1 principal cell layer or the stratum radiatum were visually identified on contralateral hemispheres of each animal. Micro-punches were made using a 0.5–10 μL pipette tip from three slices per hemisphere and pooled into ice-cold lysis buffer: 150 mM NaCl, 20 mM Tris-HCl, 1% CHAPS and protease inhibitor mixture (Roche Diagnostics). Tissue was sonicated and centrifuged at 12,000 g for 10 min. Supernatants were processed for western blotting as described below. Kv4.2 expression was normalized to β-actin for each sample.

Western blots—Sample proteins were separated on 4–12% Bis-Tris gels (ThermoFisher, NP0322) using SDS buffer (ThermoFisher, NP0002) and electrophoresis chambers (ThermoFisher, El0001). Proteins were transferred using electrophoretic chambers (Bio-Rad, 1703930) in a Tris based buffer (ThermoFisher, NP0006) to PVDF membranes (Millipore, IPFL00010). Immunoblots were blocked for 1 h at 4°C and probed using primary antibodies overnight at 4°C in Odyssey blocking buffer (Li-Cor Biosciences). After washes in PBST, immunoblots were probed for 1 h at RT with secondary antibodies conjugated to infrared dyes for detection using the Odyssey infrared imaging system (LI-COR Biosciences, Lincoln, NE). Quantification of results was performed using Odyssey software.

Immunostaining

Brain slices: Deeply anesthetized mice were transcardially perfused with ice-cold paraformaldehyde (PFA) solution (4% PFA (Electron Microscopy Sciences, 15714-S), PBS, pH 7.4). Whole brains were dissected, post-fixed in 4% PFA for 4 h, and cryopreserved with increasing concentrations of sucrose solutions (10, 20 and 30% for 4, 12, and 12–24 h respectively). Cryopreserved brains were sectioned in a cryostat at 7 mm thickness (Histoserv, Inc.) through the dorsal hippocampus beginning at −1.955 mm caudal to bregma and adhered to microscope slides (Superfrost™ Plus, ThermoFisher, 1255015) and stored at −80°C. After thawing at RT for 15 min, a circle was drawn with a pap pen around each section to create a hydrophobic barrier. Sections were rehydrated using PBS for 5 min at RT and blocked for 1 h at RT (0.3% Triton X-100, 1% normal goat serum, PBS, pH 7.3–7.4). Next, fresh blocking solution containing primary antibodies was applied and incubated 24–48 h at 4°C in a closed, humidified box. Slides were washed 4 × 15 min in PBS with agitation. Secondary antibody was applied in 0.2% Triton X-100 PBS and sections were incubated while protected from light for 2 h at RT. Sections were washed 4 × 15 min in PBS with agitation. Coverslips were mounted using a DAPI-containing mounting medium (ProLong™ Gold Antifade, ThermoFisher, P36931).

Cultured hippocampal neurons: Primary neurons grown on glass coverslips were washed 1x with PBS and fixed in PFA solution for 10 min at RT. Neurons were washed 3 × 5 min with PBS and permeabilized using 0.2% Triton X-100 for 10 min at RT. After 3 × 1 min PBS washes, neurons were blocked with 3% BSA dissolved in PBS overnight at 4°C and protected from light. Primary antibodies were applied in 3% BSA PBS for 2 h at RT with gentle agitation. Neurons were washed 3 × 1 min in PBS and secondary antibodies dissolved in PBS were incubated for 1 h at RT with gentle agitation and protected from light. After 3 × 1 min washes, coverslips were mounted face-down on glass slides in mounting medium with DAPI (ProLong™ Gold Antifade, ThermoFisher, P36931).

Confocal fluorescence microscopy and analysis—PFA-fixed neuronal cultures and mouse brain slices were imaged using a Zeiss 710 laser scanning confocal microscope running Zen Black software (Zeiss Microscopy). Fluorescence was acquired using 405/449 nm (DAPI), 488/515 nm (Alexa 488), and 633/670 (Alexa 647) nm laser excitation/emission wavelengths. Hippocampal sections were imaged on a Zeiss 10x Plan-Apochromat 10x/0.45NA air objective capturing 0.83 μm/pixel in x and y dimensions. Z-stacks were 20.83 μm tall with a 5.21 μm step size. For cultured neurons, a Zeiss 63× Plan-Apochromat/

1.4NA oil objective was used to capture 2D planes yielding 0.13 μm/pixel in *x* and *y* dimensions. Z-stacks were captured at 3.36 mm tall using 0.42 μm z-steps, and max intensity projections were used for analysis. Analysis was performed in ImageJ (NIH). Spine and dendrite fluorescence intensities were measured using ROI masks of all clearly identifiable mushroom-shaped spines and dendrite segments closest to the spine of interest. Mean fluorescence intensity of spines and dendrites for each neuron were used to generate spine/dendrite ratios. Spine/dendrite ratios were consistent across the entire range of fluorescence intensities for Cav2.3-EGFP (R^2 = 0.086)), Kv4.2-Myc (R^2 = 0.076), and mCherry (R^2 = 0.021).

Förster resonance energy transfer (FRET)

FRET Acquisition: Cultured HEK293-FT cells were trypsinized ≤ 2 min, counted, and 75,000 cells were seeded onto uncoated 18 mm glass coverslips. After 24 h growth, cells were transfected using OPTI-MEM serum free medium, X-tremeGene 9 (Sigma, 6365779001) and various plasmids. Living cells were imaged in a Tyrode's salt solution (in mM: 135 NaCl, 5 KCl, 2 $CaCl_2$, 1 $MgCl_2$, 25 HEPES, 10 glucose, pH 7.4) at RT 24–48 h post-transfection. An Observer.Z1 microscope (Zeiss) with a 63x plan-apochromat, 1.4 NA oil objective (Zeiss), Lambda LS Xenon Arc Lamp Light Source System (Sutter Instruments), AxioCam MRm camera (Zeiss), and Zen Blue software (Zeiss) were used for image acquisition. Three-filter FRET images were captured using appropriate filter cubes (Semrock) housed in the microscope turret. CFP cube: (Ex. 438/24 nm, Em. 483/32 nm, Di. 458 nm), YFP cube: (Ex. 500/24 nm, Em. 542/27 nm, Di. 520 nm), and FRET cube: (Ex. 438/24 nm, Em. 542/27 nm, Di. 458 nm). ImageJ software (NIH) was used for image processing and calculations of sensitized FRET efficiency were adapted from the method of Clemens Kaminski (Kaminski et al., 2014) with more details provided below.

FRET analysis: CFP, YFP, and CFP-YFP rawFRET fluorescence were captured in single *xy* planes using the following excitation and detection scheme: CFP image: CFP excitation and CFP emission (CFP fluorescence intensity) YFP image: YFP excitation and YFP emission (YFP fluorescence intensity) rawFRET image: CFP excitation and YFP emission (uncorrected FRET fluorescence intensity)

Fluorescence background was estimated by measuring the mean pixel values for several images captured in a cell-free section of the coverslip on the experimental day. After background subtraction, fluorescence intensity in the rawFRET image was corrected for CFP bleed-through and YFP cross-excitation. A significant percentage of the fluorescent signal in the rawFRET image was not due to FRET, but instead results from spectral crosstalk that must be subtracted. A percentage of fluorescence emission from CFP was present in the YFP emission bandpass of the rawFRET image (CFP bleed-through). Conversely, YFP cross-excitation occurs when CFP excitation bandpass in the rawFRET image leads to direct excitation of YFP. For each FRET pair, CFP bleed-through and YFP cross-excitation in the rawFRET image was measured by expressing either the CFP or YFP construct alone and determining the ratio of fluorescence intensity in the rawFRET image divided by the fluorescence intensity in the CFP (donor emission ratio (DER) or YFP (Acceptor emission ratio (AER)) image across many cells. Each FRET pair yields spectral

cross-talk that when subtracted from the rawFRET image, generates the true signal due to CFP/YFP FRET, known here as corrected FRET (FRETc). The equation

$$FRETc = rawFRET - (DER \times CFP) - (AER \times YFP)$$

was used to determine the amount of FRET in each cell. Mean $CFP, YFP,$ and raw $FRET$ fluorescence intensities were measured by mask analysis of regions enriched for the construct of interest. For cells expressing 1:1 stoichiometry of CFP and YFP, apparent $FRET$ efficiency values were calculated from mean intensities and normalized to the fraction of acceptor molecules undergoing FRET($FRET\ EFF_A$) using the equation:

$$FRET\ EFF_A = \frac{FRETc}{AER \times YFP \times \beta}$$

where β relates spectral and excitation efficiencies of donor and acceptor molecules. For experiments measuring the stoichiometry of $CFP/YFP\ FRET$ pairs, cells were transfected with various ratios of CFP and YFP cDNAs and imaged as above. In addition to measuring $FRET\ EFF_A$, $FRET\ EFF_D$ was calculated using the equation:

$$FRET\ EFF_D = \frac{FRETc\frac{a}{DER}}{CFP + FRETc\frac{\alpha}{DER}}$$

where α relates the quantum yields and signal detection efficiencies between donor and acceptors. The values for α and β were found using the method of Kaminski (Kaminski et al., 2014). Briefly, using the wide-field microscopy system described above, transfection of a control $CFP - YFP$ tandem fusion construct consisting of CFP and YFP separated by an 18 amino acid linker (GLRSRAQASNSAVEGSAM) with a predetermined FRET efficiency of 0.38 allows for determination of α and β using the following equations:

$$\alpha = \frac{0.38}{1 - 0.38}\frac{DER \times CFP}{FRETc}$$

$$\beta = \frac{FRETc}{AER \times YFP \times 0.38}$$

Plotting either $FRET\ EFF_A$ vs. CFP/YFP or $FRET\ EFF_D$ vs. YFP/CFP gives a measure of saturating $FRET$ at either the acceptor or donor. The ratio of the maximum $FRET$ value normalized for acceptor or donor concentration approximates the stoichiometry of the interaction as described by others (Chen et al., 2006a; Ben-Johny et al., 2016; Hoppe et al., 2002).

Fluorescence recovery after photo bleaching (FRAP)

FRAP acquisition: Fluorescence imaging was performed on a Zeiss 710 laser scanning confocal microscope equipped with a 405–30 nm diode laser, tunable Argon laser, DPSS 561–10 nm laser, and a Zeiss 63x Plan-Apochromat/1.4 NA oil objective. A stage insert incubation system was used to maintain cells at 34°C. Samples were illuminated at low laser power (2.0–3.5%). Image acquisition and ROI bleaching was driven by Zen Black software (Zeiss Microscopy). Images were acquired at 4X zoom yielding 0.033 μm/pixel. Cells were imaged 24–48 hrs after transfection in Tyrode's salt solution. For HEK293-FT cells, 500,000 cells were seeded onto 25 mm coverslips in 6-well cell culture dishes (Corning). After 24 h, cells were transfected with CFP, YFP, Kv4.2-CFP, or YFP-Cav2.3 constructs using X-trem-eGene 9 Transfection Reagent (Sigma-Aldrich, 06365779001). Samples were illuminated at low laser power with either 405 nm or 515 nm laser excitation, PMT gain of 700, and at 0.5 Hz. Both CFP and YFP fluorescence were photobleached within a 50 px^2 ROI using 8 iterations of the 405 nm laser at 100% power. For cultured neurons, DIV12–13 neurons were transfected with Kv4.2-sGFP2 and mCherry using Lipofectamine 2000 Transfection Reagent (ThermoFisher, 52887). Samples were illuminated with 488 nm and 560 nm laser excitation, PMT gain of 700–750, and at 0.2 Hz. Kv4.2-SGFP2 fluorescence was photobleached within a 30 px^2 ROI for dendrite shafts and a custom ROI matching the shape of each spine. Both dendrite and spine photobleaching required 8 iterations of the 405 nm laser at 100% power.

FRAP data analysis: FRAP data was processed and analyzed as previously described (Murphy et al., 2019) using the double normalization method described by Phair and Misteli (Phair and Misteli, 2000),

$$I_{norm} = \frac{ref_{pre} \times (I_{FRAP}(t) - I_{bkgd}(t))}{(I_{ref}(t) - I_{bkgd}(t)) \times frp_{pe}}$$

Where ref_{pre} and frp_{pre} are the background corrected means of the pre-bleach time points from the reference and FRAP region intensity traces, respectively. $I_{FRAP}(t)$ is the fluorescence intensity within the FRAP ROI, $I_{bkgd}(t)$ is a background intensity from an ROI outside the cell, and $I_{ref}(t)$ is the reference intensity in an unbleached region of the cell to account for photobleaching during acquisition. FRAP curves from individual ROIs were vetted for adequate bleaching (≥ 50% post-bleach intensity compared to pre-bleach intensity) and stability of intensity trace (e.g., traces with distortions due to cellular movement or stage-drift were discarded). After screening, normalized curves were then scaled 0 to 1 and averaged. Standard deviation and standard error of the mean were calculated. Averaged curves were fitted with a single-exponential, $FRAP(t) = A \times (1 - e^{-\tau \times t})$, where A is the mobile fraction using GraphPad Prism software.

HEK293-FT cell voltage clamp recordings—HEK293-FT cells were seeded onto 35 mm cell culture dishes at a concentration of 500 × 10^6 cells per dish. After 16–24 h, cultures were transfected with various plasmids (1–2 μg). To each dish, DNA was mixed with 300 μl Opti-MEM Reduced Serum Medium (ThermoFisher, 31985070) reduced serum medium. Next, 6 μl X-tremegene 9 DNA Transfection Reagent (Sigma-Aldrich, 06365779001) was

added and incubated for 10 min at room temperature before dropwise addition to cultures. On the day of recording (24–48 h after transfection), cultures were trypsinized for ≤ 2 min and seeded at low density onto glass coverslips and allowed to adhere ≥ 1 h. Coverslips were then transferred to a recording chamber and superfused (1–2 ml min^{-1}) in 95% O_2, 5% CO_2 saturated extracellular solution (in mM: 115 NaCl, 2.5 KCl, 1.25 NaH_2PO_4, 25 $NaHCO_3$, 2 $CaCl_2$, 1 $MgCl_2$, 25 glucose, pH 7.2–7.3; 300 mOsm/L) at RT. Borosilicate patch electrodes were pulled using a two-stage pipette puller (Narishige PC-10) to a tip resistance of 2.5–4.0 MΩ. Patch electrodes were filled with (in mM): 115 KCl, 10 NaCl, 20 KOH, 10 Hepes, 10 EGTA, and 25 glucose (pH 7.3, 290 mOsm). Maximum voltage-gated K^+ currents were elicited by voltage steps from a holding potential (−70 mV) to −120 mV for 400 ms to relieve Kv4.2 channel inactivation and to +60 mV for 400 ms to maximize channel opening. Inactivation rates were measured by fitting the falling phase of macroscopic currents with a double exponential decay. Voltage dependence of activation was performed using the same holding and hyperpolarizing steps as above but with a range of intermediate activation potentials (−100, −80, −60, −40, −30, −20, −10, 0, +10, +20, +30, +40, and +60 mV). Voltage-dependence of inactivation was determined using 400 ms conditioning steps from holding to −140, −130, −120, −100, −80, −60, −40, −20, −10, and 0 mV immediately before a 400 ms step to +60 mV. Recovery from inactivation was measured using two 400 ms voltage steps to +60 mV separated by various intervals (5, 10, 15, 20, 25, 50, 100, 200, and 500 ms).

Cultured neuron voltage clamp recordings—Primary hippocampal cultured neurons were grown on 12 mm coverslips to DIV6–9 for whole cell recordings or DIV21–27 for miniature excitatory postsynaptic current recordings. At the time of recording, a coverslip was transferred from a 12-well culture plate to the recording chamber and superfused in extracellular solution as described above for HEK293-FT cells. Patch electrodes were pulled as described above to a tip resistance of 5–7 MΩ and back-filled with an internal solution containing (in mM): 20 KCl, 125 K-gluconate, 5 EGTA, 4 NaCl, 4 Mg^{2+}-ATP, 0.3 Na-GTP, 10 HEPES, and 10 phosphocreatine (pH 7.2, 290 mOsm). Once whole-cell configuration was achieved, neurons were held at −60 mV between voltage protocols. I_A was evoked with a 400 ms conditioning step to −80 mV to relieve inactivation before stepping to 0 mV for 400 ms. I_A was recorded in the presence of bath applied drugs to block contaminating postsynaptic currents: (in μM) 0.5 Tetrodotoxin (TTX) (Tocris, 1069), 1.0 SR 95531 hydrobromide (Gabazine) (Tocris, 1262), 10.0 CNQX-Na^2 (Tocris, 1045), and 2.0 MK-801 maleate (Tocris, 0924) or 50 μM D-AP5 (Tocris, 0106). The voltage protocol was repeated every 5 s for 6 min. Drugs were applied by rapid perfusion (3 ml/min) 20 s after recordings began. IC_{50} for Ni^{2+} block of I_A was determined using a single exponential fit to the dose-response curve. For measurements of the voltage-dependence of inactivation, 400 ms conditioning steps from holding to −120, −100, −80, −70, −60, −50, −40, −20, −10, and 0 mV immediately before a 400 ms step to 0 mV. A Boltzmann function was fit and plotted with the voltage-dependence of inactivation data. Miniature excitatory postsynaptic currents (mEPSCs) were recorded in the presence of TTX and Gabazine. For mEPSC recordings in the presence of bath applied Ni^{2+} or AmmTX3 (Alamone Labs, STA-305), a 10 min wash-in period ensured efficient R-current and I_A block, respectively before patching. Immediately after break-in, mEPSCs were recorded in 2 min epochs at a holding potential of −70 mV.

Event amplitude was measured by the "Threshold Search" event detection procedure in Clampfit. A maximum of 200 events from each neuron were included for analysis.

Hippocampal slice preparation and recordings—6–8 week-old male mice were anesthetized with isoflurane and decapitated. For cell-attached dendritic recordings, mice were transcardially perfused with ice-cold slicing solution before decapitation. Brains were then transferred into ice-cold slicing solution containing in mM: 2.5 KCl, 28 $NaHCO_3$, 1.25 NaH_2PO_4, 7 Glucose, 0.5 $CaCl_2$, 7 $MgCl_2$, 233 Sucrose, and bubbled with 95% O2/5% CO2. Transverse slices of the hippocampus (300 μm) were made using a Leica VT1200S vibrating microtome. Slices were transferred to 32°C ACSF containing in mM: 125 NaCl, 2.5 KCl, 25 $NaHCO_3$, 1.25 NaH_2PO_4, 25 Glucose, $2CaCl_2$, 1 $MgCl_2$, 1 ascorbic acid, 3 Na-Pyruvate, and bubbled with 95% O2/5% CO2. After 25 minutes the slice chamber was transferred to room temperature for the rest of the recording day. For recording, slices were transferred to a recording-chamber with continuous flow of ACSF (2–3 ml/min). Recording pipettes for somatic whole cell and outside-out patch recordings had a tip-resistance of 3–5 MΩ and were filled with an internal solution containing in mM: 20 KCl, 125 K-Gluconate, 1 EGTA, NaCl, 4 NaCl, Mg-ATP, 0.3 NaGTP, 10 HEPES, 10 Phosphocreatine, pH 7.26, 296 mOsm. Recording pipettes for dendritic cell-attached voltage clamp were filled with an internal solution mimicking ACSF, containing in mM: 3 KCl, 125 NaCl, 10 HEPES, 25 Glucose, $2CaCl_2$, 1 $MgCl_2$, pH 7.24, 290 mOsm. Dendritic cell-attached recordings were performed in voltage clamp mode and voltage step protocols have been inverted for readability in the results section, to account for the reversed polarity of the cell-attached recordings. Protocols were designed for a theoretical resting membrane potential of −60 mV. I_A was calculated by subtracting I_{sus} from I_{tot} as previously described (Hu et al., 2020b). I_{tot} was elicited using a voltage step to +40 from a −120 mV pre-pulse and a subsequent step to +40 from −30 mV was used to isolate I_{sus}. Bath ACSF was supplemented with 1μM TTX to block voltage-gated sodium channels, 1μM Gabazine to selectively block GABAA receptors, and 10μM CNQX to block AMPA-type and Kainate-type glutamate receptors. Recording electrodes were pulled to 10–12 MΩ using a Narishige PC-10 pipette puller and polished using a Narishige microforge.

Electrophysiology data acquisition and analysis—Manual patch clamp experiments were performed on an Axioskop 2 FS Plus microscope (Zeiss) with CP-Achromat 10 × 0.25 air (Zeiss) and LumplanFL 60 ×1.0 NA water immersion (Olympus) objectives, and Sutter MPC-200 multi manipulator system with ROE-200 controller. The rig was equipped with a Sutter LB-LS/17 lamp for fluorescence and DIC optics. An Axon Multiclamp 700B amplifier, Axon Digidata 1440A A/D converter and pClamp software (Molecular Devices, Sunnyvale, CA) were used to acquire electrophysiological signals. Currents were normalized to cell size using whole-cell capacitance upon cell break-in, and leak currents were subtracted using a P/4 protocol. Data were analyzed using Microsoft Excel, MATLAB, Igor Pro (WaveMetrics, Lake Oswego, OR), and GraphPad Prism. Pooled data are presented as either bar graphs ±SEM overlaid with individual data points or in tabular format ±SEM.

Ca^{2+} imaging and analysis—Fast confocal imaging was performed using a 25 × 1.1 NA water immersion objective on an A1R MP HD system (Nikon) coupled to a Retiga

ELECTRO CCD camera (QImaging) used for sample scanning. Time-series were captured at 15.3 Hz using a 6x zoom on a resonant scanner yielding 0.08 μm/pixel. Image acquisition was controlled by Elements software (Nikon) and analysis was performed in ImageJ (NIH). DIV13–15 primary hippocampal neurons grown on 18 mm glass coverslips were transfected 24–48 h before imaging using Lipofectamine 2000. Neurons were transfected with the genetically encoded Ca^{2+} indicator GCaMP6f and mCherry as a marker of neuronal morphology. Coverslips were transferred to a quick release magnetic imaging chamber (Warner, QR-41LP) with constant perfusion (1–2 ml/min) of modified Tyrode's salt solution (3 mM $CaCl_2$, 0 mM $MgCl_2$, 10 μM glycine, 0.5 μM TTX) at RT. Variability and low event frequency required identification of spines that were active both before and after pharmacological treatments. Spine Ca^{2+} signals were analyzed by drawing a mask over the spine of interest. Mean GCaMP6f fluorescence intensity was measured using the "Plot Z-axis Profile" function in imageJ. Extracted intensity values were background-subtracted and normalized to baseline fluorescence intensity ($\Delta F/F_0$). Only a transient >2.5 fold above baseline was used for analysis. Many of the analyzed Ca^{2+} transients were clearly individual events; however, if two or more transients overlapped, we developed rules to discern whether they should be considered multiple events. For a trailing event to be considered a separate event, the initiating transient must have dropped $>50\%$ of maximum. Additionally, the trailing transient must rise $>50\%$ above the lowest $\Delta F/F_0$ of the previous spike to be considered a separate event. If a trailing transient did not meet both criteria it was not considered a separate event from the initiating transient.

QUANTIFICATION AND STATISTICAL ANALYSIS—All statistical analysis was performed using GraphPad Prism software. All statistical details for experiments can be found in the figure legends and results text. Significance was defined as $p < 0.05$. All statistical methods and p-values (unless <0.0001) can be found in the figure legends or the results text. n values can be found either in the figure panels, the figure legend, and the results text. Mean and SEM values are reported within the results text where indicated. Sample sizes were determined based on the variability observed in the first 4–5 replicates. Samples were allocated into treatment groups randomly. Controls were performed in alternation with the various treatments throughout the experimental day. For Cav2.3 KO mouse recordings, the experimenter was blinded to genotype.

Supplementary Material

Refer to Web version on PubMed Central for supplementary material.

ACKNOWLEDGMENTS

This work was supported by the Intramural Research Program of the *Eunice Kennedy Shriver* National Institute of Child Health and Human Development (ZIAHD008755 to D.A.H.) and the National Institute of General Medical Sciences Postdoctoral Research Associate Training Grant (FI2GM12004 to J.G.M.). Support was also provided by the Intramural Research Program of NIH/National Institute on Deafness and Other Communication Disorders (NIDCD) (Advanced Imaging Core-ZICDC000081 to R.S.P. and Y.-X.W.). We thank members of the Hoffman lab for valuable discussions, protocols, and experimental assistance. We would like to thank Mark Dell'Acqua for comments on this manuscript. We are grateful to Adriano Bellotti for contributing cultured rat neurons used in some of the experiments. The Ca^{2+}-dead KChIP2c construct was generated by site-directed mutagenesis by Jung Park. Ying Liu bred, genotyped, and cared for the WT and Cav2.3 KO mice used in this work. We thank Vincent Schram (NICHD Microscopy & Imaging Core) for technical assistance.

REFERENCES

An WF, Bowlby MR, Betty M, Cao J, Ling HP, Mendoza G, Hinson JW, Mattsson KI, Strassle BW, Trimmer JS, and Rhodes KJ. (2000). Modulation of A-type potassium channels by a family of calcium sensors. Nature 403, 553–556. [PubMed: 10676964]

Anderson D, Mehaffey WH, Iftinca M, Rehak R, Engbers JD, Hameed S, Zamponi GW, and Turner RW. (2010). Regulation of neuronal activity by Cav3-Kv4 channel signaling complexes. Nat. Neurosci. 13, 333–337. [PubMed: 20154682]

Andrasfalvy BK, Makara JK, Johnston D, and Magee JC. (2008). Altered synaptic and non-synaptic properties of CA1 pyramidal neurons in Kv4.2 knockout mice. J. Physiol. 586, 3881–3892. [PubMed: 18566000]

Augustine GJ, Santamaria F, and Tanaka K. (2003). Local calcium signaling in neurons. Neuron 40, 331–346. [PubMed: 14556712]

Barnwell LF, Lugo JN, Lee WL, Willis SE, Gertz SJ, Hrachovy RA, and Anderson AE. (2009). Kv4.2 knockout mice demonstrate increased susceptibility to convulsant stimulation. Epilepsia 50, 1741–1751. [PubMed: 19453702]

Beaulieu-Laroche L, and Harnett MT. (2018). Dendritic spines prevent synaptic voltage clamp. Neuron 97, 75–82.e3. [PubMed: 29249288]

Beck EJ, Bowlby M, AN WF, Rhodes KJ, and Covarrubias M. (2002). Remodelling inactivation gating of Kv4 channels by KChIP1, a small-molecular-weight calcium-binding protein. J. Physiol. 538, 691–706. [PubMed: 11826158]

Ben-Johny M, Yue DN, and Yue DT. (2016). Detecting stoichiometry of macromolecular complexes in live cells using FRET. Nat. Commun. 7, 13709. [PubMed: 27922011]

Bernard C, Anderson A, Becker A, Poolos NP, Beck H, and Johnston D. (2004). Acquired dendritic channelopathy in temporal lobe epilepsy. Science 305, 532–535. [PubMed: 15273397]

Biever A, Glock C, Tushev G, Ciirdaeva E, Dalmay T, Langer JD, and Schuman EM. (2020). Monosomes actively translate synaptic mRNAs in neuronal processes. Science 367, eaay4991.

Bloodgood BL, Giessel AJ, and Sabatini BL. (2009). Biphasic synaptic Ca influx arising from compartmentalized electrical signals in dendritic spines. PLoS Biol. 7, e1000190. [PubMed: 19753104]

Bloodgood BL, and Sabatini BL. (2007). Nonlinear regulation of unitary synaptic signals by CaV(2.3) voltage-sensitive calcium channels located in dendritic spines. Neuron 53, 249–260. [PubMed: 17224406]

Cai X, Liang CW, Muralidharan S, Kao JP, Tang CM, and Thompson SM. (2004). Unique roles of SK and Kv4.2 potassium channels in dendritic integration. Neuron 44, 351–364. [PubMed: 15473972]

Cajigas IJ, Tushev G, Will TJ, Tom Dieck S, Fuerst N, and Schuman EM. (2012). The local transcriptome in the synaptic neuropil revealed by deep sequencing and high-resolution imaging. Neuron 74, 453–466. [PubMed: 22578497]

Callsen B, Isbrandt D, Sauter K, Hartmann LS, Pongs O, and Bahring R. (2005). Contribution of N- and C-terminal Kv4.2 channel domains to KChIP interaction [corrected]. J. Physiol. 568, 397–412. [PubMed: 16096338]

Cash S, and Yuste R. (1998). Input summation by cultured pyramidal neurons is linear and position-independent. J. Neurosci. 18, 10–15. [PubMed: 9412481]

Cash S, and Yuste R. (1999). Linear summation of excitatory inputs by CA1 pyramidal neurons. Neuron 22, 383–394. [PubMed: 10069343]

Chen H, Puhl HL 3r.d., Koushik SV, Vogel SS, and Ikeda SR. (2006a). Measurement of FRET efficiency and ratio of donor to acceptor concentration in living cells. Biophys. J. 91, L39–L41. [PubMed: 16815904]

Chen QX, and Wong RK. (1991). Intracellular Ca2+ suppressed a transient potassium current in hippocampal neurons. J. Neurosci. 11, 337–343. [PubMed: 1992004]

Chen X, Yuan LL, Zhao C, Birnbaum SG, Frick A, Jung WE, Schwarz TL, Sweatt JD, and Johnston D. (2006b). Deletion of Kv4.2 gene eliminates dendritic A-type K+ current and enhances induction of long-term potentiation in hippocampal CA1 pyramidal neurons. J. Neurosci. 26, 12143–12151. [PubMed: 17122039]

Craig TA, Benson LM, Venyaminov SY, Klimtchuk ES, Bajzer Z, Prendergast FG, Naylor S, and Kumar R. (2002). The metal-binding properties of DREAM: evidence for calcium-mediated changes in DREAM structure. J. Biol. Chem. 277, 10955–10966. [PubMed: 11788589]

Forster T. (1948). Zwischenmolekulare Energiewanderung und Fluoreszenz. Ann. Phys. 437, 55–75.

Gardoni F, Mauceri D, Marcello E, Sala C, Di Luca M, and Jeromin A. (2007). SAP97 directs the localization of Kv4.2 to spines in hippocampal neurons: regulation by CaMKII. J. Biol. Chem. 282, 28691–28699. [PubMed: 17635915]

Gray EE, Murphy JG, Liu Y, Trang I, Tabor GT, Lin L, and Hoffman DA. (2019). Disruption of GpI mGluR-dependent Cav2.3 translation in a mouse model of fragile X syndrome. J. Neurosci. 39, 7453–7464. [PubMed: 31350260]

Groen C, and Bahring R. (2017). Modulation of human Kv4.3/KChIP2 channel inactivation kinetics by cytoplasmic Ca(2). Pflugers Arch. 469, 1457–1470. [PubMed: 28735419]

Gross C, Yao X, Pong DL, Jeromin A, and Bassell GJ. (2011). Fragile X mental retardation protein regulates protein expression and mRNA translation of the potassium channel Kv4.2. J. Neurosci. 31, 5693–5698. [PubMed: 21490210]

Grunditz A, Holbro N, Tian L, Zuo Y, and Oertner TG. (2008). Spine neck plasticity controls postsynaptic calcium signals through electrical compartmentalization. J. Neurosci. 28, 13457–13466. [PubMed: 19074019]

Guglielmi L, Servettini I, Caramia M, Catacuzzeno L, Franciolini F, D'adamo MC, and Pessia M. (2015). Update on the implication of potassium channels in autism: K (+) channelautism spectrum disorder. Front. Cell. Neurosci. 9, 34. [PubMed: 25784856]

Gutzmann JJ, Lin L, and Hoffman DA. (2019). Functional coupling of Cav2.3 and BK potassium channels regulates action potential repolarization and short-term plasticity in the mouse hippocampus. Front. Cell. Neurosci. 13, 27. [PubMed: 30846929]

Hall AM, Throesch BT, Buckingham SC, Markwardt SJ, Peng Y, Wang Q, Hoffman DA, and Roberson ED. (2015). Tau-dependent Kv4.2 depletion and dendritic hyperexcitability in a mouse model of Alzheimer's disease. J. Neurosci. 35, 6221–6230. [PubMed: 25878292]

Hammond RS, Lin L, Sidorov MS, Wikenheiser AM, and Hoffman DA. (2008). Protein kinase a mediates activity-dependent Kv4.2 channel trafficking. J. Neurosci. 28, 7513–7519. [PubMed: 18650329]

Hoffman DA, and Johnston D. (1998). Downregulation of transient K+ channels in dendrites of hippocampal CA1 pyramidal neurons by activation of PKA and PKC. J. Neurosci. 18, 3521–3528. [PubMed: 9570783]

Hoffman DA, Magee JC, Colbert CM, and Johnston D. (1997). K+ channel regulation of signal propagation in dendrites of hippocampal pyramidal neurons. Nature 387, 869–875. [PubMed: 9202119]

Holmqvist MH, Cao J, Hernandez-Pineda R, Jacobson MD, Carroll KI, Sung MA, Betty M, Ge P, Gilbride KJ, Brown ME, et al. (2002). Elimination of fast inactivation in Kv4 A-type potassium channels by an auxiliary subunit domain. Proc. Natl. Acad. Sci. U S A 99, 1035–1040. [PubMed: 11805342]

Holmqvist MH, Cao J, Knoppers MH, Jurman ME, Distefano PS, Rhodes KJ, Xie Y, and An WF. (2001). Kinetic modulation of Kv4-mediated A-current by arachidonic acid is dependent on potassium channel interacting proteins. J. Neurosci. 21, 4154–4161. [PubMed: 11404400]

Hoppe A, Christensen K, and Swanson JA. (2002). Fluorescence resonance energy transfer-based stoichiometry in living cells. Biophys. J. 83, 3652–3664. [PubMed: 12496132]

Hu JH, Malloy C, and Hoffman DA. (2020a). P38 regulates kainic acid-induced seizure and neuronal firing via Kv4.2 phosphorylation. Int. J. Mol. Sci. 21, 5921. [PubMed: 32824677]

Hu JH, Malloy C, Tabor GT, Gutzmann JJ, Liu Y, Abebe D, Karlsson RM, Durell S, Cameron HA, and Hoffman DA. (2020b). Activity-dependent isomerization of Kv4.2 by Pin1 regulates cognitive flexibility. Nat. Commun. 11, 1567. [PubMed: 32218435]

Jerng HH, and Pfaffinger PJ. (2008). Multiple Kv channel-interacting proteins contain an N-terminal transmembrane domain that regulates Kv4 channel trafficking and gating. J. Biol. Chem. 283, 36046–36059. [PubMed: 18957440]

Jerng HH, and Pfaffinger PJ. (2014). Modulatory mechanisms and multiple functions of somatodendritic A-type K (+) channel auxiliary subunits. Front. Cell Neurosci 8, 82. [PubMed: 24723849]

Johnston D, Christie BR, Frick A, Gray R, Hoffman DA, Schexnayder LK, Watanabe S, and Yuan LL. (2003). Active dendrites, potassium channels and synaptic plasticity. Philos. Trans. R. Soc. Lond. B Biol. Sci. 358, 667–674. [PubMed: 12740112]

Kaminski CF, Rees EJ, and Schierle GS. (2014). A quantitative protocol for intensity-based live cell FRET imaging. Methods Mol. Biol. 1076, 445–454.

Kerti K, Lorincz A, and Nusser Z. (2012). Unique somato-dendritic distribution pattern of Kv4.2 channels on hippocampal CA1 pyramidal cells. Eur. J. Neurosci. 35, 66–75. [PubMed: 22098631]

Kim J, Jung S, Clemens A, Petralia R, and Hoffman DA. (2007). Regulation of dendritic excitability by activity-dependent trafficking of the A-Type K+ channel subunit Kv4.2 in hippocampal neurons. Neuron 54, 933–947. [PubMed: 17582333]

Kim J, Wei DS, and Hoffman DA. (2005). Kv4 potassium channel subunits control action potential repolarization and frequency-dependent broadening in rat hippocampal CA1 pyramidal neurones. J. Physiol. 569, 41–57. [PubMed: 16141270]

Kimm T, and Bean BP. (2014). Inhibition of A-type potassium current by the peptide toxin SNX-482. J. Neurosci. 34, 9182–9189. [PubMed: 25009251]

Kise Y, Kasuya G, Okamoto HH, Yamanouchi D, Kobayashi K, Kusakizako T, Nishizawa T, Nakajo K, and Nureki O. (2021). Structural basis of gating modulation of Kv4 channel complexes. Nature 599, 158–164. [PubMed: 34552243]

Kitazawa M, Kubo Y, and Nakajo K. (2014). The stoichiometry and biophysical properties of the Kv4 potassium channel complex with K+ channel-interacting protein (KChIP) subunits are variable, depending on the relative expression level. J. Biol. Chem. 289, 17597–17609. [PubMed: 24811166]

Kremers GJ, Goedhart J, van den Heuvel DJ, Gerritsen HC, and Gadella TW Jr. (2007). Improved green and blue fluorescent proteins for expression in bacteria and mammalian cells. Biochemistry 46, 3775–3783. [PubMed: 17323929]

Kunjilwar K, Qian Y, and Pfaffinger PJ. (2013). Functional stoichiometry underlying KChIP regulation of Kv4.2 functional expression. J. Neurochem. 126, 462–472. [PubMed: 23692269]

Lakowicz JR. (2006). Principles of Fluorescence Spectroscopy (Springer).

Lin L, Sun W, Kung F, Dell'acqua ML, and Hoffman DA. (2011). AKAP79/150 impacts intrinsic excitability of hippocampal neurons through phosphoregulation of A-type K+ channel trafficking. J. Neurosci. 31, 1323–1332. [PubMed: 21273417]

Lockridge A, and Yuan LL. (2011). Spatial learning deficits in mice lacking A-type K(+) channel subunits. Hippocampus 21, 1152–1156. [PubMed: 20857488]

Maffie JK, Dvoretskova E, bougis PE, Martin-Eauclaire MF, and Rudy B. (2013). Dipeptidyl-peptidase-like-proteins confer high sensitivity to the scorpion toxin AmmTX3 to Kv4-mediated A-type K+ channels. J. Physiol. 591, 2419–2427. [PubMed: 23440961]

Magee JC, Christofi G, Miyakawa H, Christie B, Lasser-Ross N, and Johnston D. (1995). Subthreshold synaptic activation of voltage-gated Ca2+ channels mediates a localized Ca2+ influx into the dendrites of hippocampal pyramidal neurons. J. Neurophysiol. 74, 1335–1342. [PubMed: 7500154]

Magee JC, and Johnston D. (1995). Characterization of single voltage-gated Na+ and Ca2+ channels in apical dendrites of rat CA1 pyramidal neurons. J. Physiol. 487, 67–90. [PubMed: 7473260]

Maletic-Savatic M, Lenn NJ, and Trimmer JS. (1995). Differential spatiotemporal expression of K+ channel polypeptides in rat hippocampal neurons developing in situ and in vitro. J. Neurosci. 15, 3840–3851. [PubMed: 7751950]

Massone S, Vassallo I, Castelnuovo M, Fiorino G, Gatta E, Robello M, Borghi R, Tabaton M, Russo C, Dieci G, et al. (2011). RNA polymerase III drives alternative splicing of the potassium channel-interacting protein contributing to brain complexity and neurodegeneration. J. Cell Biol. 193, 851–866. [PubMed: 21624954]

Megias M, Emri Z, Freund TF, and Gulyas AI. (2001). Total number and distribution of inhibitory and excitatory synapses on hippocampal CA1 pyramidal cells. Neuroscience 102, 527–540. [PubMed: 11226691]

Metz AE, Jarsky T, Martina M, and Spruston N. (2005). R-type calcium channels contribute to afterdepolarization and bursting in hippocampal CA1 pyramidal neurons. J. Neurosci. 25, 5763–5773. [PubMed: 15958743]

Metzbower SR, Joo Y, Benavides DR, and Blanpied TA. (2019). Properties of individual hippocampal synapses influencing NMDA-receptor activation by spontaneous neurotransmission. eNeuro 6 (3), ENEURO.0126–19.2019.

Monaghan MM, Menegola M, Vacher H, Rhodes KJ, and Trimmer JS. (2008). Altered expression and localization of hippocampal A-type potassium channel subunits in the pilocarpine-induced model of temporal lobe epilepsy. Neuroscience 156, 550–562. [PubMed: 18727953]

Morohashi Y, Hatano N, Ohya S, Takikawa R, Watabiki T, Takasugi N, Imaizumi Y, Tomita T, and Iwatsubo T. (2002). Molecular cloning and characterization of CALP/KChIP4, a novel EF-hand protein interacting with presenilin 2 and voltage-gated potassium channel subunit Kv4. J. Biol. Chem. 277, 14965–14975. [PubMed: 11847232]

Murphy JG, Crosby KC, Dittmer PJ, Sather WA, and Dell'acqua ML. (2019). AKAP79/150 recruits the transcription factor NFAT to regulate signaling to the nucleus by neuronal L-type Ca(2+) channels. Mol. Biol. Cell 30, 1743–1756. [PubMed: 31091162]

Murphy JG, and Hoffman DA. (2019). A polybasic motif in alternatively spliced KChIP2 isoforms prevents Ca (2+) regulation of Kv4 channels. J. Biol. Chem. 294, 3683–3695. [PubMed: 30622142]

Murthy VN, Sejnowski TJ, and Stevens CF. (2000). Dynamics of dendritic calcium transients evoked by quantal release at excitatory hippocampal synapses. Proc. Natl. Acad. Sci. U S A 97, 901–906. [PubMed: 10639177]

Nadal MS, Ozaita A, Amarillo Y, Vega-Saenz de Miera E, Ma Y, Mo W, Goldberg EM, Misumi Y, Ikehara Y, Neubert TA, and Rudy B. (2003). The CD26-related dipeptidyl aminopeptidase-like protein DPPX is a critical component of neuronal A-type K+ channels. Neuron 37, 449–461. [PubMed: 12575952]

Naraghi M, and Neher E. (1997). Linearized buffered Ca2+ diffusion in microdomains and its implications for calculation of [Ca2+] at the mouth of a calcium channel. J. Neurosci. 17, 6961–6973. [PubMed: 9278532]

Nicholson DA, Trana R, Katz Y, Kath WL, Spruston N, and Geinisman Y. (2006). Distance-dependent differences in synapse number and AMPA receptor expression in hippocampal CA1 pyramidal neurons. Neuron 50, 431–442. [PubMed: 16675397]

Oliveria SF, Gomez LL, and Dell'Acqua ML. (2003). Imaging kinase– AKAP79–phosphatase scaffold complexes at the plasma membrane in living cells using FRET microscopy. J. Cell Biol. 160, 101–112. [PubMed: 12507994]

Osawa M, Tong KI, Lilliehook C, Wasco W, Buxbaum JD, Cheng HY, Penninger JM, Ikura M, and Ames JB. (2001). Calcium-regulated DNA binding and oligomerization of the neuronal calcium-sensing protein, calsenilin/DREAM/KChIP3. J. Biol. Chem. 276, 41005–41013. [PubMed: 11535596]

Parajuli LK, Nakajima C, Kulik A, Matsui K, Schneider T, Shigemoto R, and Fukazawa Y. (2012). Quantitative regional and ultrastructural localization of the Ca(v)2.3 subunit of R-type calcium channel in mouse brain. J. Neurosci. 32, 13555–13567. [PubMed: 23015445]

Patel SP, Campbell DL, and Strauss HC. (2002). Elucidating KChIP effects on Kv4.3 inactivation and recovery kinetics with a minimal KChIP2 isoform. J. Physiol. 545, 5–11. [PubMed: 12433945]

Patriarchi T, Buonarati OR, and Hell JW. (2018). Postsynaptic localization and regulation of AMPA receptors and Cav1.2 by beta2 adrenergic receptor/PKA and Ca(2+)/CaMKII signaling. EMBO J. 37, e99771. [PubMed: 30249603]

Petralia RS, and Wang Y-X. (2021). Review of post-embedding immunogold methods for the study of neuronal structures. Front. Neuroanat. 15, 763427. [PubMed: 34720893]

Phair RD, and Misteli T. (2000). High mobility of proteins in the mammalian cell nucleus. Nature 404, 604–609. [PubMed: 10766243]

Pioletti M, Findeisen F, Hura GL, and Minor DL Jr. (2006). Three-dimensional structure of the KChIP1-Kv4.3 T1 complex reveals a cross-shaped octamer. Nat. Struct. Mol. Biol. 13, 987–995. [PubMed: 17057713]

Reese AL, and Kavalali ET. (2015). Spontaneous neurotransmission signals through store-driven Ca(2+) transients to maintain synaptic homeostasis. Elife 4, e09262. [PubMed: 26208337]

Rhodes KJ, Carroll KI, Sung MA, Doliveira LC, Monaghan MM, Burke SL, Strassle BW, Buchwalder L, Menegola M, Cao J, et al. (2004). KChIPs and Kv4 alpha subunits as integral components of A-type potassium channels in mammalian brain. J. Neurosci. 24, 7903–7915. [PubMed: 15356203]

Schneider CA, Rasband WS, and Eliceiri KW. (2012). NIH Image to ImageJ: 25 years of image analysis. Nat. Methods 9, 671–675. [PubMed: 22930834]

Schrader LA, Anderson AE, Mayne A, Pfaffinger PJ, and Sweatt JD. (2002). PKA modulation of Kv4.2-encoded A-type potassium channels requires formation of a supramolecular complex. J. Neurosci. 22, 10123–10133. [PubMed: 12451113]

Seifert C, Storch S, and Bahring R. (2020). Modulation of Kv4.2/KChIP3 interaction by the ceroid lipofuscinosis neuronal 3 protein CLN3. J. Biol. Chem. 295, 12099–12110. [PubMed: 32641494]

Seikel E, and Trimmer JS. (2009). Convergent modulation of Kv4.2 channel alpha subunits by structurally distinct DPPX and KChIP auxiliary subunits. Biochemistry 48, 5721–5730. [PubMed: 19441798]

Seong HJ, Behnia R, and Carter AG. (2014). Impact of subthreshold membrane potential on synaptic responses at dendritic spines of layer 5 pyramidal neurons in the prefrontal cortex. J. Neurophysiol. 111, 1960–1972. [PubMed: 24478153]

Shah MM, Hammond RS, and Hoffman DA. (2010). Dendritic ion channel trafficking and plasticity. Trends Neurosci. 33, 307–316. [PubMed: 20363038]

Sheng M, Tsaur ML, Jan YN, and Jan LY. (1992). Subcellular segregation of two A-type K+ channel proteins in rat central neurons. Neuron 9, 271–284. [PubMed: 1497894]

Shibata R, Misonou H, Campomanes CR, Anderson AE, Schrader LA, Doliveira LC, Carroll KI, Sweatt JD, Rhodes KJ, and Trimmer JS. (2003). A fundamental role for KChIPs in determining the molecular properties and trafficking of Kv4.2 potassium channels. J. Biol. Chem. 278, 36445–36454. [PubMed: 12829703]

Singh B, Ogiwara I, Kaneda M, Tokonami N, Mazaki E, Baba K, Matsuda K, Inoue Y, and Yamakawa K. (2006). A Kv4.2 truncation mutation in a patient with temporal lobe epilepsy. Neurobiol. Dis. 24, 245–253. [PubMed: 16934482]

Stuart G, Spruston N, and Hä Usser M. (2016). Dendrites (Oxford University Press).

Sun W, Maffie JK, Lin L, Petralia RS, Rudy B, and Hoffman DA. (2011). DPP6 establishes the A-type K(+) current gradient critical for the regulation of dendritic excitability in CA1 hippocampal neurons. Neuron 71, 1102–1115. [PubMed: 21943606]

Takahashi H, and Magee JC. (2009). Pathway interactions and synaptic plasticity in the dendritic tuft regions of CA1 pyramidal neurons. Neuron 62, 102–111. [PubMed: 19376070]

Ulbrich MH, and Isacoff EY. (2007). Subunit counting in membrane-bound proteins. Nat. Methods 4, 319–321. [PubMed: 17369835]

Vacher H, Alami M, Crest M, Possani LD, Bougis PE, and Martin-Eauclaire MF. (2002). Expanding the scorpion toxin alpha-KTX 15 family with AmmTX3 from Androctonus mauretanicus. Eur. J. Biochem. 269, 6037–6041. [PubMed: 12473099]

Varga AW, Anderson AE, Adams JP, Vogel H, and Sweatt JD. (2000). Input-specific immunolocalization of differentially phosphorylated Kv4.2 in the mouse brain. Learn. Mem. 7, 321–332. [PubMed: 11040264]

Varga AW, Yuan LL, Anderson AE, Schrader LA, Wu GY, Gatchel JR, Johnston D, and Sweatt JD. (2004). Calcium-calmodulin-dependent kinase II modulates Kv4.2 channel expression and upregulates neuronal A-type potassium currents. J. Neurosci. 24, 3643–3654. [PubMed: 15071113]

Walker AS, Neves G, Grillo F, Jackson RE, Rigby M, O'donnell C, Lowe AS, Vizcay-Barrena G, Fleck RA, and Burrone J. (2017). Distance-dependent gradient in NMDAR-driven spine calcium signals along tapering dendrites. Proc. Natl. Acad. Sci. U S A 114, E1986–E1995. [PubMed: 28209776]

Wang H, Yan Y, Liu Q, Huang Y, Shen Y, Chen L, Chen Y, Yang Q, Hao Q, Wang K, and Chai J. (2007). Structural basis for modulation of Kv4 K+ channels by auxiliary KChIP subunits. Nat. Neurosci. 10, 32–39. [PubMed: 17187064]

Wang HG, He XP, Li Q, Madison RD, Moore SD, Mcnamara JO, and Pitt GS. (2013). The auxiliary subunit KChIP2 is an essential regulator of homeostatic excitability. J. Biol. Chem. 288, 13258–13268. [PubMed: 23536187]

Wang K, Kelley MH, Wu WW, Adelman JP, and Maylie J. (2015). Apamin boosting of synaptic potentials in CaV2.3 R-type Ca2+ channel null mice. PLoS One 10, e0139332. [PubMed: 26418566]

Wang K, Lin MT, Adelman JP, and Maylie J. (2014). Distinct Ca2+ sources in dendritic spines of hippocampal CA1 neurons couple to SK and Kv4 channels. Neuron 81, 379–387. [PubMed: 24462100]

Wang X, Bao J, Zeng XM, Liu Z, and Mei YA. (2005). Elevation of intracellular Ca2+ modulates A-currents in rat cerebellar granule neurons. J. Neurosci. Res. 81, 530–540. [PubMed: 15957157]

Watanabe S, Hoffman DA, Migliore M, and Johnston D. (2002). Dendritic K+ channels contribute to spike-timing dependent long-term potentiation in hippocampal pyramidal neurons. Proc. Natl. Acad. Sci. U S A 99, 8366–8371. [PubMed: 12048251]

Williams ME, Marubio LM, Deal CR, Hans M, Brust PF, Philipson LH, Miller RJ, Johnson EC, Harpold MM, and Ellis SB. (1994). Structure and functional characterization of neuronal alpha 1E calcium channel subtypes. J. Biol. Chem. 269, 22347–22357. [PubMed: 8071363]

Wilson SM, Toth PT, Oh SB, Gillard SE, Volsen S, Ren D, Philipson LH, Lee EC, Fletcher CF, Tessarollo L, et al. (2000). The status of voltage-dependent calcium channels in alpha 1E knock-out mice. J. Neurosci. 20, 8566–8571. [PubMed: 11102459]

Wong W, Newell EW, Jugloff DG, Jones OT, and Schlichter LC. (2002). Cell surface targeting and clustering interactions between heterologously expressed PSD-95 and the Shal voltage-gated potassium channel, Kv4.2. J. Biol. Chem. 277, 20423–20430. [PubMed: 11923279]

Yuan LL, Adams JP, Swank M, Sweatt JD, and Johnston D. (2002). Protein kinase modulation of dendritic K+ channels in hippocampus involves a mitogen-activated protein kinase pathway. J. Neurosci. 22, 4860–4868. [PubMed: 12077183]

Highlights

- Cav2.3 R-type voltage-gated Ca^{2+} channels are coupled to Kv4.2 A-type K^{+} channels
- Cav2.3-Kv4.2 complexes are localized to dendrites and spines of CA1 pyramidal neurons
- Cav2.3-mediated Ca^{2+} influx promotes Kv4.2 functional expression in dendrites
- Cav2.3 regulates Kv4.2-mediated attenuation of spontaneous synaptic input

A

Position	Cav2.3 Peptide	Δcorr	Xcorr
19-30	SLFIFGEDNIVR	0.148	2.48
352-362	NSGTSALEVLR	0.174	2.03
403-410	VDGASYFR	0.141	1.94
809-822	GDIGGLTSVLDNQR	0.345	2.90
1516-1528	LVNTSGFNMSFLK	0.052	2.19
1869-1884	ALPYLQQDPVSGLSGR	0.504	4.22
1938-1950	SNSSWLEEFSMER	0.402	2.76

Protein	Number of peptides (Unique)	Number of peptides (Total)	% of aa sequence coverage
Kv4.2	96	386	67.30%
Kv4.1	21	35	31.07%
Kv4.3	25	33	37.56%
DPP6	7	8	9.78%
DPP10	2	2	2.14%
KChIP1	8	20	30.84%
KChIP2	7	8	27.04%
KChIP3	4	9	25.00%
KChIP4	8	16	33.20%
Cav2.3	7	7	3.80%

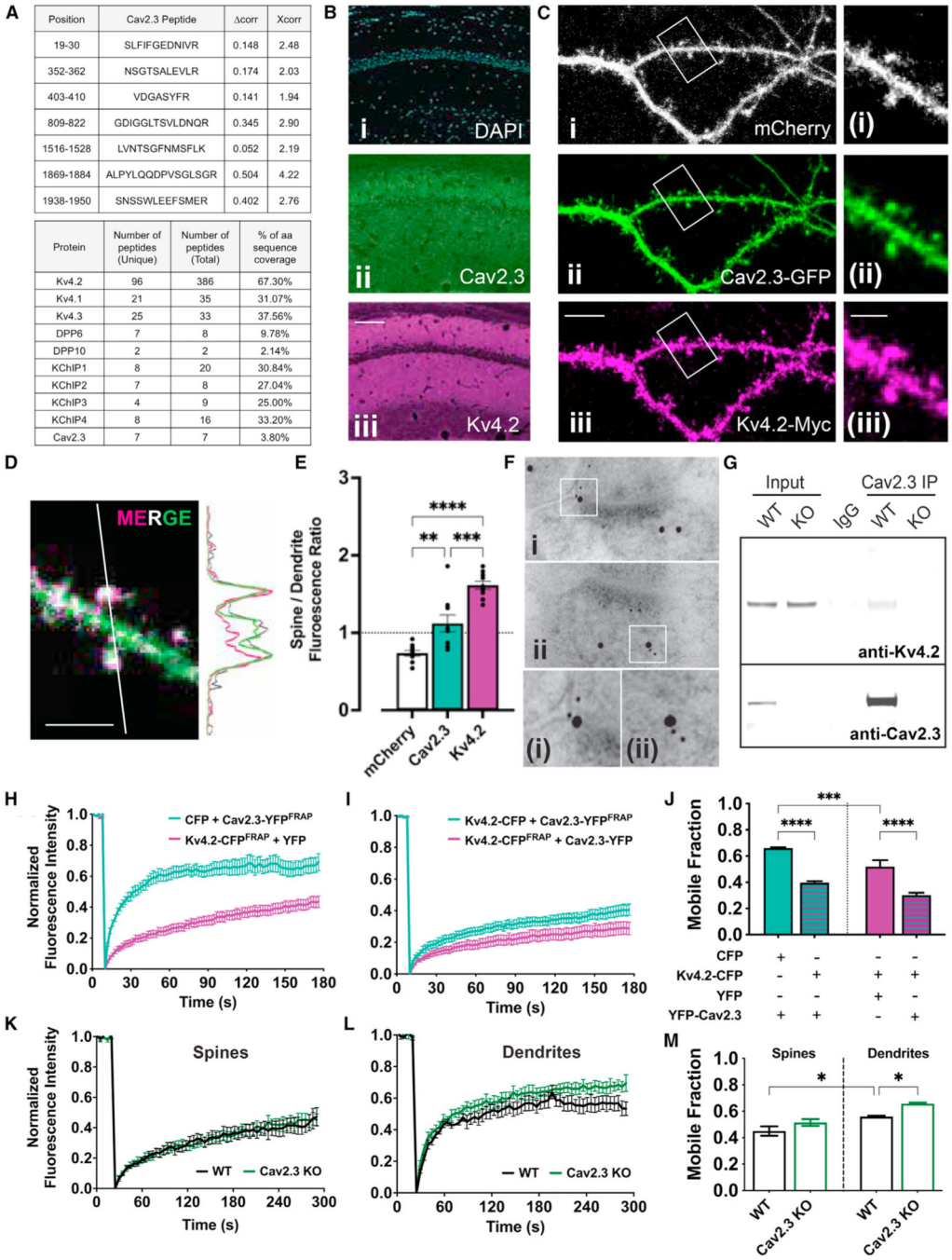

Figure 1. Cav2.3 and Kv4.2 voltage-gated ion channel subunits form a protein complex in the rodent hippocampus

(A) Top: Peptide coverage for the Cav2.3 protein sequence in Kv4.2 TAP-MS experiments. Xcorr: Sequest cross-correlation score; Δcorr: Xcorr difference between the top-ranked and next-best sequence. Bottom: Table of Kv4.x, DPPx, and KChIPx TAP hits confirming known Kv4.x interactions in Kv4.2 TAP-MS experiments. The numbers of specific and total peptides are shown and the percent amino acid sequence coverage for each protein are shown.

(B) Mouse hippocampal brain sections were stained for (Bi) nuclei (DAPI), (Bii) Cav2.3, and (Biii) Kv4.2 channels. Cav2.3 and Kv4.2 are localized to dendrite fields of hippocampal area CA1; 100 μm scale bar.

(C) Dispersed cultured rat hippocampal neurons expressing (Ci, white) mCherry, (Cii, green) Cav2.3-GFP, and (Ciii, purple) Kv4.2-myc. (Inset) Cav2.3 and Kv4.2 channel fluorescence was enriched in dendritic spines relative to mCherry; 10 μm and 3 μm scale bars.

(D) Merged Kv4.2-myc and Cav2.3-GFP fluorescence of dendritic segment in (C). The representative intensity profile shows enrichment of both Cav2.3-GFP and Kv4.2-myc in spines; 3 μm scale bar.

(E) Cav2.3-GFP and Kv4.2-myc are enriched in spines when compared to cytosolic mCherry; n = 10.

(F) Double immunogold electron micrographs of rat area CA1 hippocampal sections labeled using 5 nm (Cav2.3) and 15 nm gold (Kv4.2). (Insets) Cav2.3 and Kv4.2 colocalize within postsynaptic spines.

(G) Kv4.2 coimmunoprecipitates with Cav2.3 from hippocampal tissue from WT but not Cav2.3 KO mouse; n = 4 biological replicates.

(H) FRAP curves obtained from HEK293-FT cells transfected with either YFP and Kv4.2-CFP (purple) or YFP-Cav2.3 (green) and CFP. Fluorescence recovery within the bleached volume was plotted over time for Kv4.2-CFP and YFP-Cav2.3 when expressed with non-interacting fluorescent proteins (YFP and CFP, respectively).

(I) FRAP curves from HEK293-FT cells expressing Kv4.2-CFP and YFP-Cav2.3 after simultaneous CFP/YFP photobleaching.

(J) Exponential functions were fit to FRAP curves, and the mobile fraction for each transfection condition was plotted. The mobile fraction plotted for either YFP-Cav2.3 (cyan) or Kv4.2-CFP (magenta) are color-coded in the bar graph. Coexpression of Kv4.2-CFP and YFP-Cav2.3 reduces respective mobile fractions consistent with reciprocal interactions between the 2 channels (n = 15–19 cells for each condition across 3 experiments).

(K) FRAP curves of spine-localized Kv4.2-SGFP2 expressed in dispersed cultures of WT (black) or Cav2.3 KO (green) mouse hippocampal neurons.

(L) FRAP curves of Kv4.2-SGFP2 localized to dendrite shafts and plotted as in (K).

(M) Bar graph comparison of Kv4.2-sGFP2 mobile fraction between WT and Cav2.3 KO mouse neurons. Subcellular comparison showed a significantly greater Kv4.2-SGFP2 mobile fraction in dendrites compared to spines. Kv4.2-SGFP2 mobile fraction was greater in dendrites of Cav2.3 KO mouse neurons when compared to WT; n = 17–18 spines and 14–17 dendrites from 7 WT and 7 Cav2.3 KO neurons.

Data were pooled from 2–3 hippocampal cultures. Error bars represent ±SEMs. Statistical significance was evaluated by 1-way ANOVA with Tukey's multiple comparisons test. *$p < 0.05$, **$p < 0.01$, ***$p < 0.001$, ****$p < 0.0001$. See also Figures S1, S2, S3, and S7.

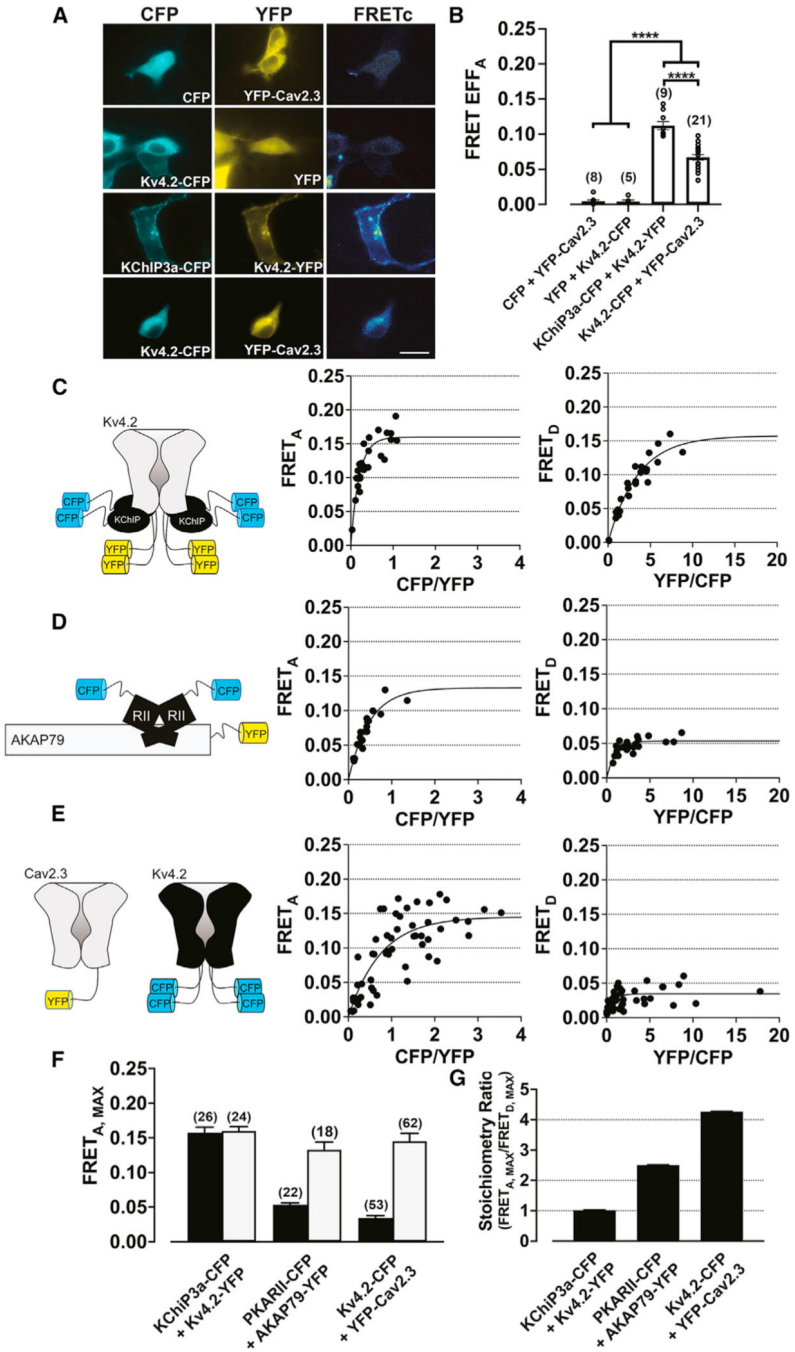

Figure 2. Cav2.3 and Kv4.2 bind at equimolar stoichiometry within a nanodomain

(A) Representative raw CFP (cyan), YFP (yellow), and FRETc (temperature spectrum pseudocolor) fluorescent images of HEK293-FT cells expressing FRET constructs at equimolar concentrations.

(B) Bar graphs show comparison of mean FRET efficiency normalized to acceptor concentration for each condition. Parentheses indicate n values from 2–3 independent experiments.

(C–E) Left, illustrations depict the expected stoichiometry of Kv4.2-YFP and KChIP2c-CFP (1:1) and AKAP79-YFP and PKARIIa-CFP (1:2), while YFP-Cav2.3 and Kv4.2-CFP stoichiometry was inferred from the data. Right: Cells were transfected with various ratios of plasmid DNA. Donor- and acceptor-normalized FRET efficiency were plotted for each cell over the ratio of donor and acceptor fluorescence.

(F) Bar graphs compare acceptor- (gray bars) and donor- (black bars) normalized FRET efficiency for each condition. Parentheses indicate n values from 2–3 biological replicates.

(G) FRET stoichiometry ratio was calculated using the formula $FRET_{A,MAX}/FRET_{D,MAX}$ was plotted for FRET pairs confirming a 1:4 ratio of acceptor:donor or a 1:1 channel stoichiometry due to the tetrameric structure of Kv4.2.

Error bars represent ±SEMs. Statistical significance was evaluated by 1-way ANOVA with Tukey's multiple comparisons test. ****$p < 0.0001$.

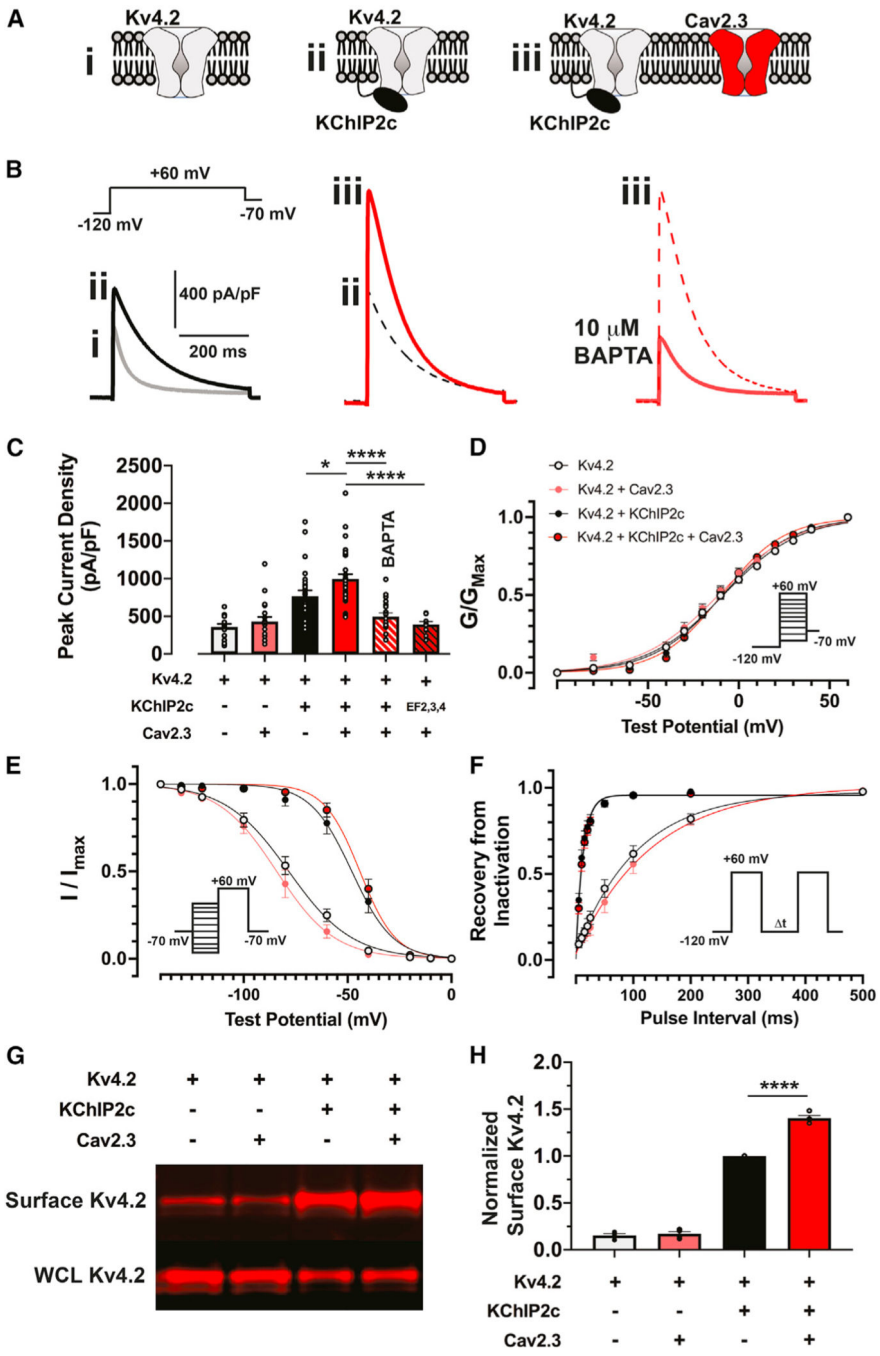

Figure 3. Cav2.3 expression increases Kv4.2 current density in a KChIP- and Ca^{2+}-dependent manner in HEK293-FT cells

(A) Illustrations depict a subset of transfection conditions with either Kv4.2 alone (i), Kv4.2 and KChIP2c (ii), or Kv4.2, KChIP2c, and Cav2.3 (iii).

(B) Representative traces from conditions shown in (A).

(C) Bar graphs plot peak Kv4.2 current density under the conditions shown. Cav2.3 expression increases Kv4.2 current density in a KChIP-dependent manner, which was reversed by the replacement of EGTA with BAPTA in the patch pipette and by coexpression of EF-dead KChIP2c.

(D) Kv4.2 voltage dependence of activation was plotted using normalized conductance against a range of membrane test potentials, and a Boltzmann function was fit and plotted with the data.
(E) Kv4.2 voltage dependence of inactivation was plotted using normalized current against conditioning test potentials, and a Boltzmann function was fit and plotted with the data.
(F) Kv4.2 recovery from inactivation was plotted as the fraction of current recovered using a +60-mV test potential from an initial test potential of the same magnitude against various recovery intervals.
(G) Representative Western blot of a surface biotinylation assay in COS-7 cells transfected according to the indicated conditions. WCL, whole-cell lysate.
(H) Bar graph shows Kv4.2 surface expression normalized to the Kv4.2 and KChIP2c expression condition. Error bars represent ±SEMs from 4 biological replicates. Statistical significance was evaluated by 1-way ANOVA with Tukey's multiple comparisons test. *$p < 0.05$, ****$p < 0.0001$.
See also Figures S3 and S7 and Table S1.

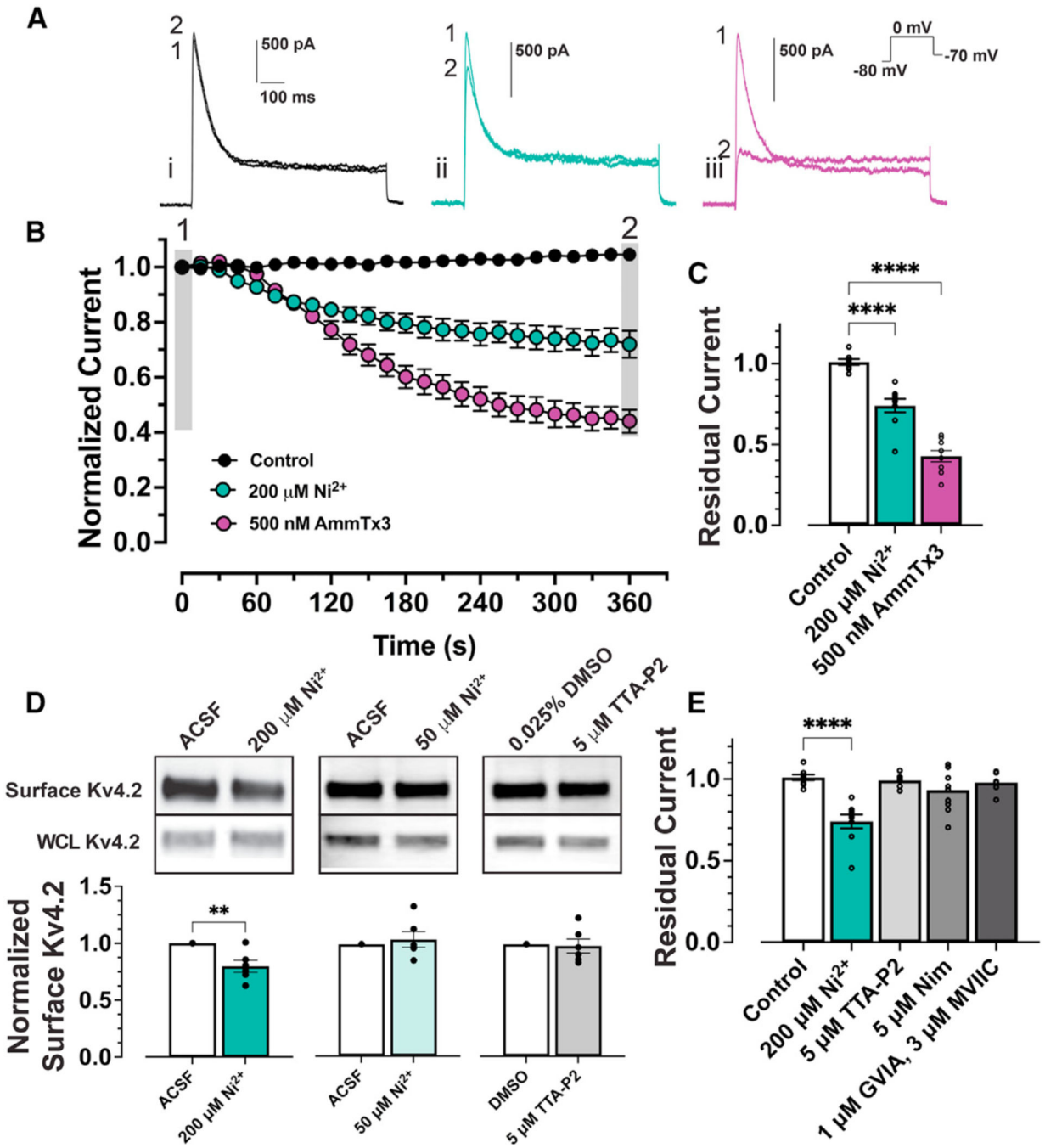

Figure 4. Cav2.3 regulates I_A and Kv4.2 surface localization in hippocampal neurons

(A) Representative whole-cell voltage clamp currents recorded from DIV 7–9 dispersed cultured rat hippocampal neurons. After obtaining whole-cell configuration, neurons were either (i) untreated and superfused with artificial cerebrospinal fluid (ACSF) or rapidly exchanged into ACSF containing (ii) 200 μM Ni^{2+} or (iii) 500 nM AmmTx3. First (1) and last (2) traces in the 6-min time course are shown.

(B) Averaged peak outward current normalized to current at break-in was plotted against the duration of the experiment. Drug wash-in began at 15 s.

(C) Peak residual current amplitude remaining at the end of the recording period was normalized to current at break-in and plotted for each condition.
(D) Representative surface biotinylation and western blot of DIV 7 dispersed rat hippocampal cultures. Endogenous Kv4.2 surface expression was reduced following a 10-min incubation in ACSF supplemented with 200 μM Ni^{2+} when compared to non-treated neurons. Neurons treated with 50 μM Ni^{2+}, a concentration more selective for Cav3.x or the Cav3.x-specific blocker TTA-P2, showed no effect on surface Kv4.2.
(E) Residual transient current was plotted after treatments with neuronal Cav3.x (5 μM TTA-P2), Cav1.x (5 μM nimodipine), and Cav2.1/Cav2.2 (1 μM ω-conotoxin GVIA/5 μM ω-conotoxin MVIIC) blockers. Note that data from (C) were reused for comparison. Error bars represent ±SEMs. Statistical significance was evaluated by either Student's t test or 1-way ANOVA with Tukey's multiple comparisons test. **$p < 0.01$, ****$p < 0.0001$.
See also Figures S5–S7.

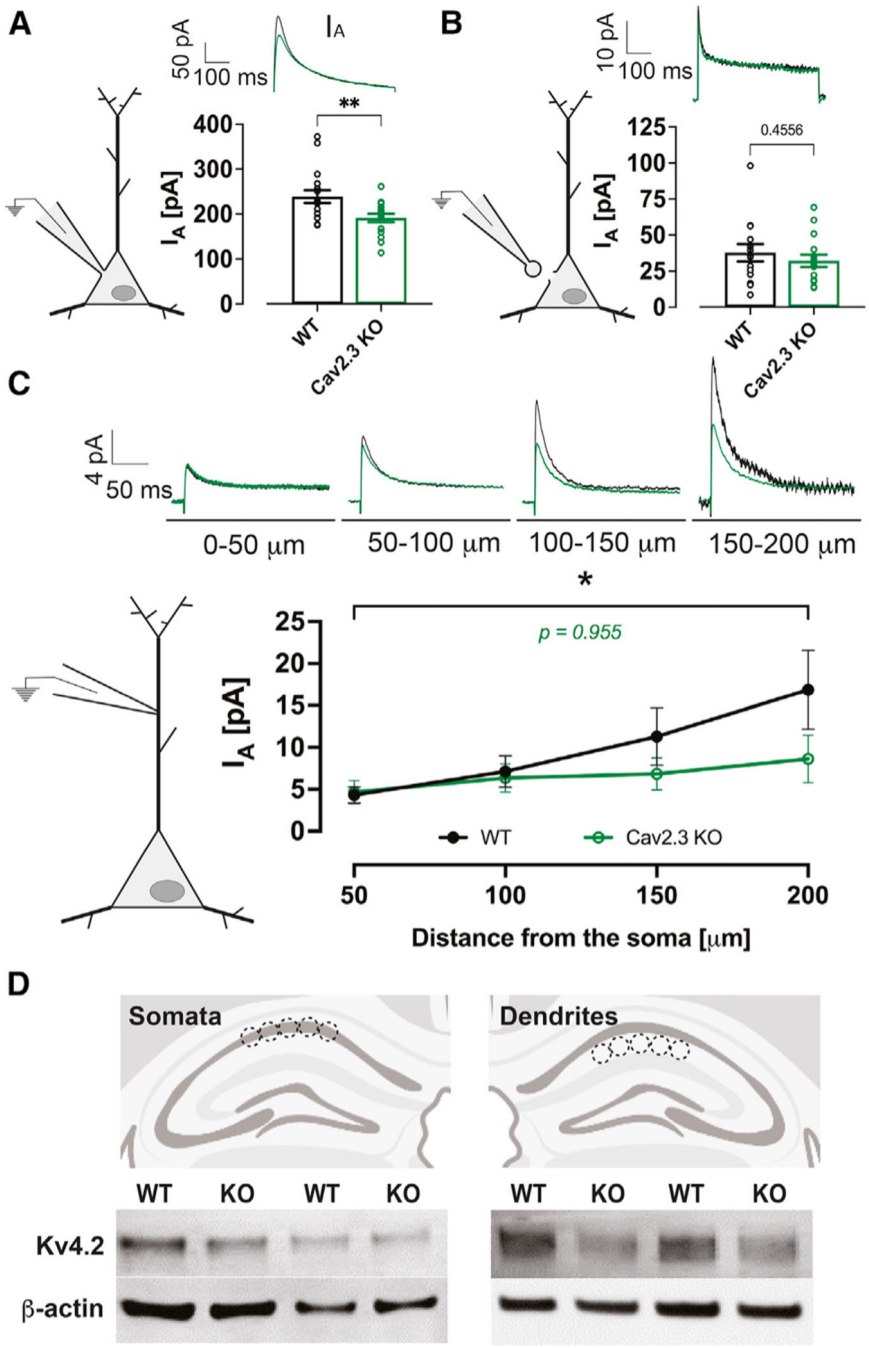

Figure 5. The I_A gradient is disrupted in Cav2.3 KO CA1 pyramidal neuron dendrites

(A) Comparison of whole-cell I_A amplitude in WT (black) and Cav2.3 KO (green) mouse; n = 17 WT and 16 KO cells. Representative I_A recordings for WT and Cav2.3 KO are shown.

(B) Comparison of I_A in outside-out somatic patches of WT and Cav2.3 KO; n = 14 WT and 15 KO cells. Representative I_A recordings are shown using averaged data.

(C) Top: Representative cell-attached I_A recordings from the apical dendrites of WT and Cav2.3 KO neurons at various distances from the neuronal cell body. Bottom: I_A was plotted

for dendrite segments. The I_A gradient was significantly reduced in Cav2.3 KO dendrites relative to WT.

(D) Micro-punch extraction of CA1 cell body layer and stratum radiatum hippocampal subregions followed by western blot detection of Kv4.2 subunit expression revealed a reduced quantity of Kv4.2 in only the dendrite layers of Cav2.3 KO relative to WT mice. Error bars represent ±SEMs. Statistical significance was evaluated by either Student's t-test or 1-way ANOVA with Tukey's multiple comparisons test. *$p < 0.05$, **$p < 0.01$.

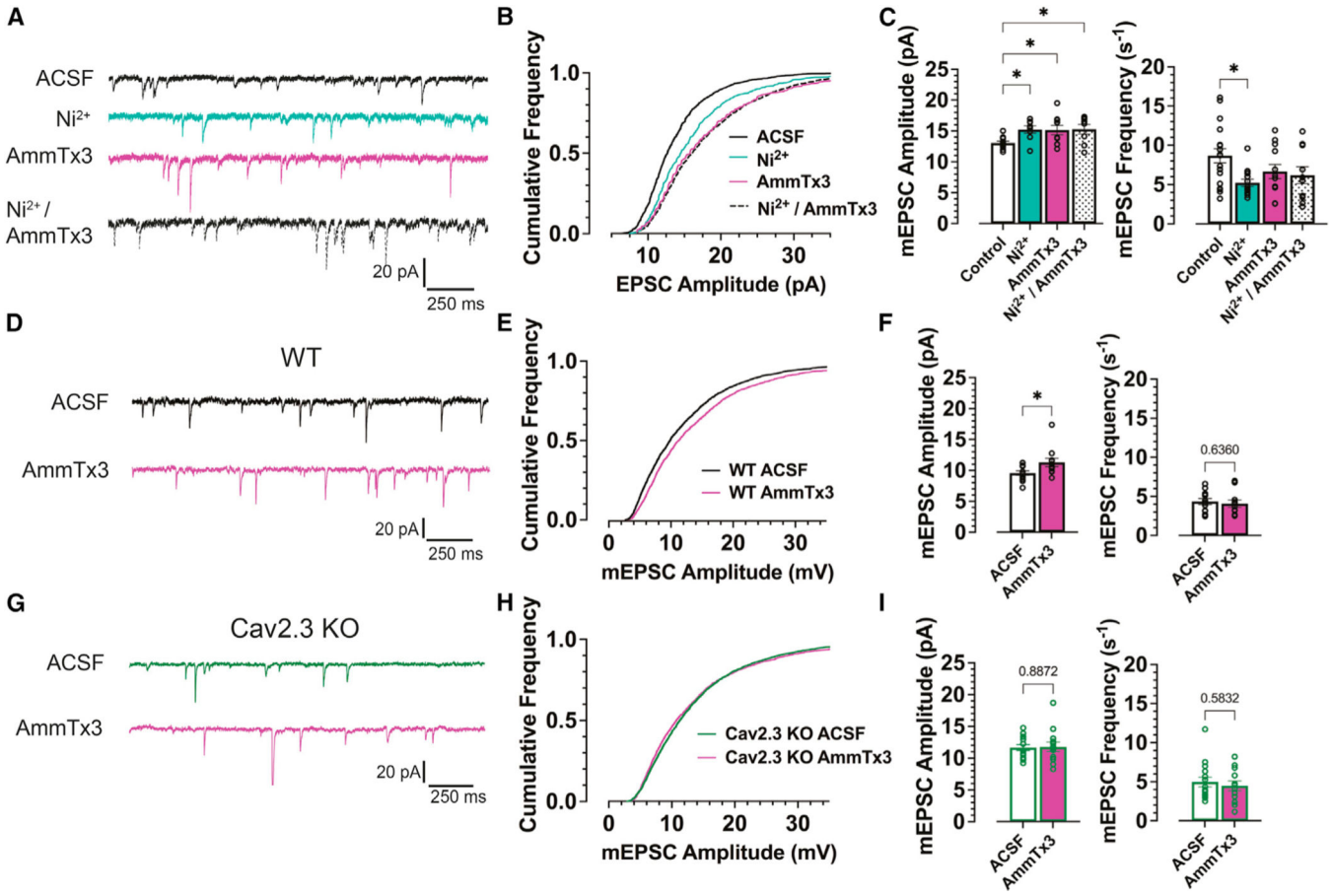

Figure 6. Cav2.3 promotes I_A-mediated attenuation of spontaneous miniature excitatory postsynaptic currents

(A) Representative miniature excitatory postsynaptic currents (mEPSCs) recorded from dispersed rat hippocampal cultures at a holding potential of —70 mV in the absence (black trace) or presence of Ni^{2+} (green), AmmTx3 (purple), or Ni^{2+} and AmmTx3 combined (hashed trace).

(B) The cumulative distribution of mEPSC amplitudes. Distribution of mEPSCs in the absence (n = 1,685) or presence of Ni^{2+} (n = 754), AmmTx3 (n = 638), or Ni^{2+} and AmmTx3 in combination (n = 1,305) are shifted toward a higher proportion of larger events.

(C) Mean median event amplitude (left) and mean frequency (right) from each neuron were compared. AmmTx3, Ni^{2+}, and Ni^{2+}/AmmTx3 increases median amplitude. However, there was no additive effect of Ni^{2+} and AmmTx3. Mean mEPSC frequency was decreased in the presence of Ni^{2+}.

(D) Representative mEPSCs recorded from WT mouse neurons in the absence (black trace) or presence (purple trace) of AmmTx3.

(E) Cumulative frequency distribution of WT mEPSCs (ACSF: n = 2,304; AmmTx3: n = 2,042). AmmTx3 induces a rightward shift in mEPSC amplitudes.

(F) Bar graphs are plotted as in (C) AmmTx3 increases mEPSC amplitudes as in WT mice.

(G–I) Cav2.3 KO mEPSCs recorded and summarized as in (D)–(F) (ACSF: n = 3,058; AmmTx3: n = 2,241). AmmTx3 had no effect on mEPSC amplitude in Cav2.3 KO neurons.

Error bars represent ±SEMs. Statistical significance was evaluated by unpaired t test or 1-way ANOVA with Tukey's multiple comparisons test. *$p < 0.05$.

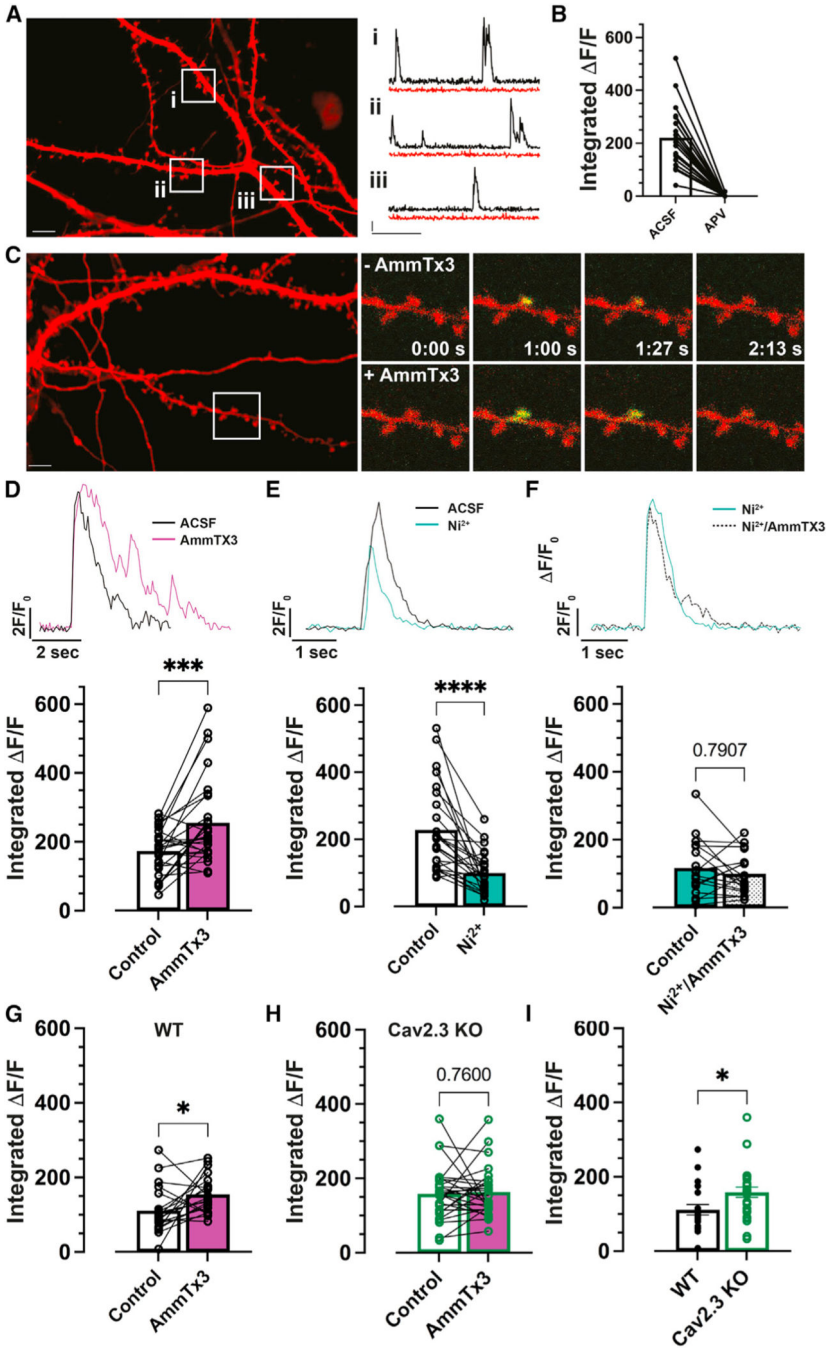

Figure 7. Cav2.3 promotes I_A-mediated attenuation of spontaneous quantal spine Ca^{2+} signals

(A) Left: A representative cultured rat hippocampal neuron expressing mCherry (red) and GCaMP6f (not shown). Scale bar: 10 μm. Right: Spontaneous spine Ca^{2+} transients in 3 representative spines (i, ii, and iii). Traces plot the magnitude of GCaMP6f fluorescence ($\Delta F/F_0$) over time for each spine before (black traces) and after a 10-min application of D-AP5 (50 μM) (red traces). Scale bar: y = 2 Δ F/F_0; x = 10s.

(B) The Ca^{2+} integral for spines (n = 19, 3 cells) was plotted before and after application of D-AP5.

(C) Left: A neuron transfected as in (A), but treated with AmmTx3 (500 nM). Right: Time-lapse images of a representative spine before (above) and after (below) AmmTx3 treatment. Scale bar: 10 μm.

(D–F) Top: The magnitude of GCaMP6f fluorescence ($\Delta F/F_0$) over time in a representative spine was plotted before and after the indicated drug treatment. Bottom: Integrated Ca^{2+} influx was plotted for spines before and after the indicated conditions. AmmTx3: n = 27; Ni^{2+}: n = 25; Ni^{2+}/AmmTx3: n = 18.

(G) AmmTx3 treatment increased spine Ca^{2+} influx in WT neurons (n = 20).

(H) AmmTx3 does not enhance spine Ca^{2+} signals in Cav2.3 KO neurons (n = 27).

(I) Basal spine Ca^{2+} transients are increased in Cav2.3 KO neurons.

Statistical significance was evaluated by paired or unpaired t tests. *p < 0.05, ***p < 0.001, ****p < 0.0001.

KEY RESOURCES TABLE

REAGENT or RESOURCE	SOURCE	IDENTIFIER
Antibodies		
Goat anti-Guinea Pig, Alexa Fluor 488	ThermoFisher	Cat#A11073; RRID: AB_2534117
Goat anti-Rabbit, Alexa Fluor 488	ThermoFisher	Cat#A1100B; RRID: AB_143165
Goat anti-Mouse, Alexa Fluor 555	ThermoFisher	Cat#A21422; RRID: AB_2535B44
Goat anti-Mouse, Alexa Fluor 647	ThermoFisher	Cat#A21236; RRID: AB_2535B05
Goat anti-Mouse, Alexa Fluor 680	ThermoFisher	Cat#A21057; RRID: AB_2535723
Goat anti-Rabbit, IRDye 800CW	Li-Cor Biosciences	Cat#926-32211; RRID: AB_2651127
Guinea Pig anti-Cav2.3	Akos Kulik (Parajuli et al., 2012)	N/A
Mouse anti-Cav2.3 (clone 62C10)	Synaptic Systems	Cat#152-441; RRID: AB_2619B47
Mouse anti-Kv4.2 (clone K57/1)	NeuroMab	Cat#75-016; RRID: AB_2B772B1
Mouse anti-Myc (clone 9E10)	Millipore Sigma	Cat#M4439; RRID: AB_439694
Rabbit anti-GFP	ThermoFisher	Cat#A11122; RRID: AB_221569
Chemicals, peptides, and recombinant proteins		
AmmTx3	Alamone Labs	Cat#STA-305
Tetrodotoxin	Tocris	Cat#1069
SR 95531 hydrobromide (Gabazine)	Tocris	Cat#1262
MK-B01 maleate	Tocris	Cat#0924
CNQX	Tocris	Cat#1045
D-AP5	Tocris	Cat#0106
Critical commercial assays		
TAP Purification Kit	Agilent Technologies	Cat#240107
Experimental models: Cell lines		
Homo sapiens: HEK293-FT	ThermoFisher	R70007; RRID: CVCL_6911
Cercopithecus aethiops: COS-7	ATCC	Cat#CRL-1651; RRID: CVCL_0224
Experimental models: Organisms/strains		
Mouse: C57BL/6J	Jackson Laboratory	Cat#0006664; RRID: IMSR_JAX:000664
Mouse: Cav2.3$^{-/-}$	Richard Miller (Wilson et al., 2000)	N/A
Rat: Sprague Dawley	Taconic Biosciences	Cat#Sprague Dawley®, SD
Recombinant DNA		
Cav2.3-GFP	Ehud Isacoff; (Ulbrich and Isacoff, 2007)	CCDS: 55664.1
YFP-Cav2.3	This paper	CCDS: 55664.1
pcDNA3-DPP6S	Bernardo Rudy	N/A
Kv4.2-GFP	Dax Hoffman; (Kim et al., 2007)	CCDS: 29974.1
Kv4.2-CFP	This paper	CCDS: 29974.1

REAGENT or RESOURCE	SOURCE	IDENTIFIER
Kv4.2-YFP	This paper	CCDS: 29974.1
Kv4.2-SGFP2	This paper	CCDS: 29974.1
Kv4.2-Myc-DDK	Origene	Cat#RC215266
pCMV-KChIP2c	Paul Pfaffinger	GenBank: AF269285.1
KChIP2c-EFmut	This paper	N/A
KChIP2c-CFP	This paper	GenBank: AF269285.1
AKAP79-YFP	Mark Dell'Acqua (Oliveria et al., 2003)	GenBank: NP_004848.3
PKARII-CFP	Mark Dell'Acqua (Oliveria et al., 2003)	GenBank: NP_032950.1
GCaMP6f	Douglas Kim & GENIE Project	Addgene 40755
CFP-18aa-YFP	Clemens Kaminski (Kaminski et al., 2014)	N/A
SGFP2-C1	Dorus Gadella; (Kremers et al., 2007)	Addgene 22881
SGFP2-N1	This paper	N/A
mCherry-N1	Takara Bio	Cat#632523
Software and algorithms		
Igor Pro	WaveMetrics, Inc.	www.wavemetrics.com
Imagej	Schneider et al., 2012	imagej.nih.gov/ij
pCLAMP	Molecular Devices	www.moleculardevices.com
Prism 9	GraphPad Software, LLC.	www.graphpad.com